Article

Cell Reports

Discrimination of Dormant and Active Hematopoietic Stem Cells by G_0 Marker Reveals Dormancy Regulation by Cytoplasmic Calcium

Graphical Abstract

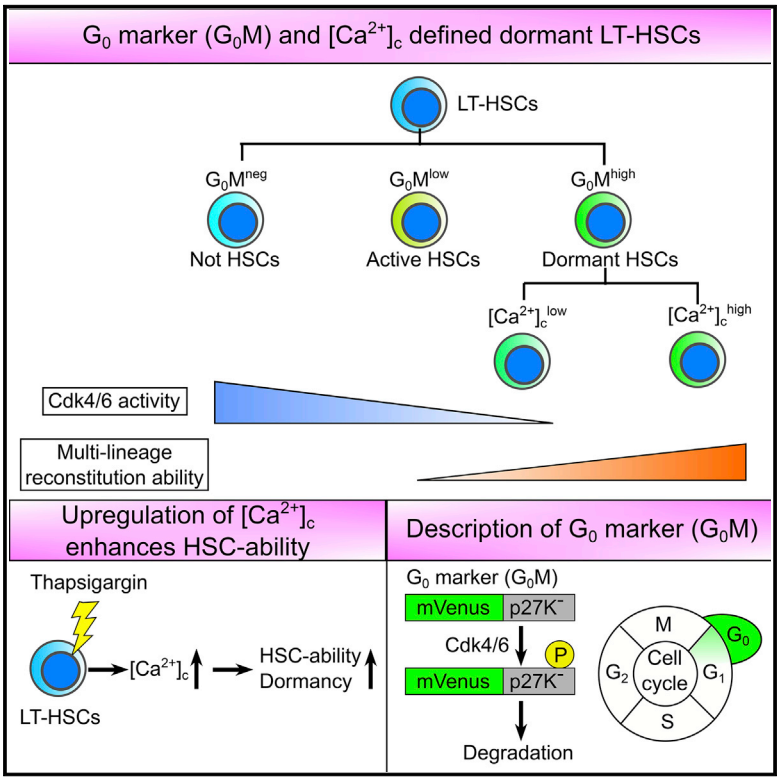

Highlights

- G_0 marker (G_0M) discriminates between dormant (G_0M^{high}) and active (G_0M^{low}) HSCs
- Active (G_0M^{low}) HSCs exhibit higher CDK4/6 activity than dormant (G_0M^{high}) HSCs
- $[Ca^{2+}]_c^{high}$ HSCs have higher bone marrow reconstitution ability than $[Ca^{2+}]_c^{low}$ HSCs
- Upregulation of $[Ca^{2+}]_c$ enhances bone marrow reconstitution ability of HSCs

Authors

Tsuyoshi Fukushima, Yosuke Tanaka, Fiona K. Hamey, ..., Hiroaki Honda, Berthold Göttgens, Toshio Kitamura

Correspondence

ytims@ims.u-tokyo.ac.jp

In Brief

Fukushima et al. show that G_0 marker (G_0M) discriminates between dormant and active HSCs within the conventional quiescent HSC fraction. Small-molecule screening reveals that high $[Ca^{2+}]_c$ is linked to dormancy of HSCs. Moreover, upregulation of $[Ca^{2+}]_c$ by thapsigargin enhances the bone marrow reconstitution ability of HSCs.

Fukushima et al., 2019, Cell Reports *29*, 4144–4158
December 17, 2019
https://doi.org/10.1016/j.celrep.2019.11.061

CellPress

OPEN ACCESS
CellPress

Cell Reports
Article

Discrimination of Dormant and Active Hematopoietic Stem Cells by G_0 Marker Reveals Dormancy Regulation by Cytoplasmic Calcium

Tsuyoshi Fukushima,[1] Yosuke Tanaka,[1,11,*] Fiona K. Hamey,[2] Chih-Hsiang Chang,[3] Toshihiko Oki,[1,4,5,6] Shuhei Asada,[1] Yasutaka Hayashi,[1] Takeshi Fujino,[1] Taishi Yonezawa,[1] Reina Takeda,[1] Kimihito Cojin Kawabata,[1,7] Tomofusa Fukuyama,[1] Terumasa Umemoto,[8] Keiyo Takubo,[9] Hitoshi Takizawa,[8] Susumu Goyama,[1] Yasushi Ishihama,[3] Hiroaki Honda,[10] Berthold Göttgens,[2] and Toshio Kitamura[1]

[1]Division of Cellular Therapy, The Institute of Medical Science, The University of Tokyo, Minato-ku, Tokyo 108-8639, Japan
[2]Department of Haematology, Wellcome Trust and MRC Cambridge Stem Cell Institute and Cambridge Institute for Medical Research, Cambridge University, Cambridge CB2 0XY, UK
[3]Department of Molecular and Cellular BioAnalysis, Graduate School of Pharmaceutical Sciences, Sakyo-ku, Kyoto University, Kyoto 606-8501, Japan
[4]Center for Regenerative Medicine, Massachusetts General Hospital, Boston, MA 02114, USA
[5]Harvard Stem Cell Institute, Cambridge, MA 02138, USA
[6]Department of Stem Cell and Regenerative Biology, Harvard University, Cambridge, MA 02138, USA
[7]Department of Hematology/Oncology, Weill Cornell Medical College, New York, NY 10021, USA
[8]International Research Center for Medical Sciences, Chuo-ku, Kumamoto University, Kumamoto 860-0811, Japan
[9]Department of Stem Cell Biology, Research Institute, National Center for Global Health and Medicine, Shinjuku-ku, Tokyo 162-8655, Japan
[10]Field of Human Disease Models, Major in Advanced Life Sciences and Medicine, Tokyo Women's Medical University, Shinjuku-ku, Tokyo 162-8666, Japan
[11]Lead Contact
*Correspondence: ytims@ims.u-tokyo.ac.jp
https://doi.org/10.1016/j.celrep.2019.11.061

SUMMARY

Quiescent hematopoietic stem cells (HSCs) are typically dormant, and only a few quiescent HSCs are active. The relationship between "dormant" and "active" HSCs remains unresolved. Here we generate a G_0 marker (G_0M) mouse line that visualizes quiescent cells and identify a small population of active HSCs (G_0M^{low}), which are distinct from dormant HSCs (G_0M^{high}), within the conventional quiescent HSC fraction. Single-cell RNA-seq analyses show that the gene expression profiles of these populations are nearly identical but differ in their Cdk4/6 activity. Furthermore, high-throughput small-molecule screening reveals that high concentrations of cytoplasmic calcium ($[Ca^{2+}]_c$) are linked to dormancy of HSCs. These findings indicate that G_0M separates dormant and active adult HSCs, which are regulated by Cdk4/6 and $[Ca^{2+}]_c$. This G_0M mouse line represents a useful resource for investigating physiologically important stem cell subpopulations.

INTRODUCTION

In some adult tissues, stem cells are present in two states: dormant and active. Dormant stem cells serve as a reserve pool of stem cells, which produce differentiated cells only in response to disturbances, such as tissue injury, whereas active stem cells contribute to differentiated cells homeostatically. Hematopoietic stem cells (HSCs) are able to give rise to all blood cell lineages and possess self-renewal potential (Seita and Weissman, 2010). HSCs also exhibit both dormant and active states (Bernitz et al., 2016; Cabezas-Wallscheid et al., 2017; Rodriguez-Fraticelli et al., 2018; Sun et al., 2014; Takizawa et al., 2011; van der Wath et al., 2009). However, despite their importance in the regulation of HSC self-renewal and differentiation, the mechanisms regulating HSC dormant and active states remain largely unknown.

Cdk6 is one of the important factors for transition from dormant to active states in HSCs (Cabezas-Wallscheid et al., 2017). The amount of CDK6 protein has been shown to be associated with cell cycle entry of human quiescent short-term HSCs (ST-HSCs) (Laurenti et al., 2015). Although these reports showed that CDK6 is important for cell cycle priming, it remains unresolved how CDK6 regulates dormant and active states in HSCs.

Calcium signaling and flux have also been shown to be important for cell cycle activation of dormant HSCs in stress hematopoiesis (Sugimura et al., 2012; Umemoto et al., 2018). The concentrations of cytoplasmic calcium ($[Ca^{2+}]_c$) have been shown to be higher in $CD150^{high}$ HSCs than $CD150^{low}$ HSCs in the steady-state condition (Luchsinger et al., 2016), although the $[Ca^{2+}]_c$ of HSCs in a steady-state condition is lower than $[Ca^{2+}]_c$ under stress conditions. Thus, the precise role of $[Ca^{2+}]_c$ and calcium influx in modulating stem cell dormancy/activity in steady-state condition is currently unknown.

Previously, we generated a fusion protein between the fluorescent protein mVenus and $p27K^-$, which is p27 lacking Cdk inhibitory activity (mVenus-$p27K^-$) as a G_0 marker (G_0M) (Oki et al., 2014). $p27K^-$ behaves in the same way as wild-type p27 except

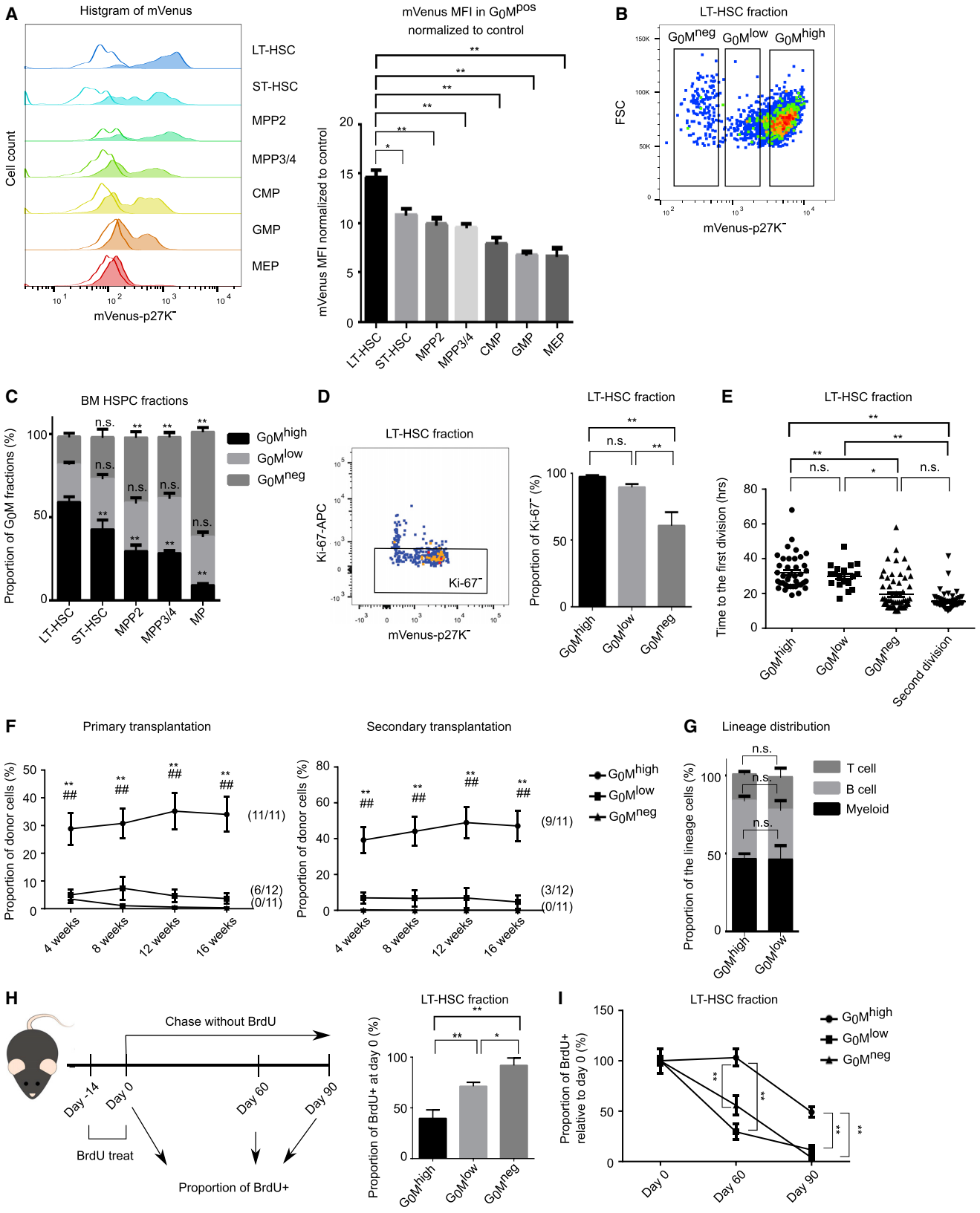

(legend on next page)

for its interaction to Cdks. p27K$^-$ does not affect cell cycle progression, because of a lack of interaction to Cdks. Thus, we can use p27K$^-$ as a reporter together with mVenus. To examine the quiescent state of HSCs in detail *in vivo*, we generated *Vav1-Cre; Rosa*$^{R26R\text{-}G0M/\ R26R\text{-}wt}$ mice, in which the quiescent state in hematopoietic cells is visualized by expression of mVenus. Using these mice, we showed that G_0M discriminates between dormant (G_0M^{high}) and active (G_0M^{low}) HSCs by Cdk4/6 activity. We also found that high $[Ca^{2+}]_c$ is linked to HSC dormancy in the steady-state condition. The G_0M mouse line established in this study will be a powerful tool for a broad range of stem cell research.

RESULTS

Generation of a G_0M Mouse Line for Hematopoietic Lineage

To visualize G_0 phase of hematopoietic cells *in vivo*, we generated a Cre-inducible *mVenus-p27K*$^-$ mouse line in which *mVenus-p27K*$^-$ was inserted into the *Rosa26* locus with a loxP-flanking Neo-cassette (Figure S1A). To generate an experimental model examining G_0M expression in HSCs, G_0M mice were crossed with *Vav1-Cre* mice, in which G_0M was expressed specifically in hematopoietic cells (hereafter referred to hG_0 mice). The hG_0 mice showed normal hematopoiesis, cell cycle, and bone marrow (BM) reconstitution potential (Figures S1B–S1D and S2A–S2D). Using hG_0 mice, we analyzed G_0M expression in hematopoietic cells. The intensity of G_0M varied among cell types. The intensity of G_0M in long-term HSCs (LT-HSCs) (CD150$^+$CD48$^-$c-Kit$^+$Sca-1$^+$Lineage marker-negative cells) was higher than in other HSPCs (hematopoietic stem/progenitor cells; c-Kit$^+$Sca-1$^+$Lineage marker-negative cells) in the BM (Figure 1A). Moreover, G_0M discriminated LT-HSCs into G_0M^{high}, G_0M^{low}, and G_0M^{neg} populations (Figure 1B). The proportion of G_0M^{high} in LT-HSCs was highest among HSPCs in the BM, consistent with the fact that most HSCs in BM are quiescent (Figure 1C). On the other hand, the proportion of G_0M^{high} was lower in fetal liver LT-HSCs than in BM LT-HSCs, consistent with the fact that fetal liver LT-HSCs are rapidly cycling (Figure S2E). The proportion of G_0M^{high} in mature blood cells from hematopoietic organs was higher than that in immature blood cells from BM and thymus (Figure S2E). These results indicate that G_0M clearly labels G_0 phase in hematopoietic lineages. Importantly, G_0M could divide G_0 phase into at least three subgroups by their intensity, indicating that the G_0M mouse line may serve as a useful tool for studying G_0 phase in more detail.

Characterization of G_0M in HSCs

To further evaluate G_0M, we examined its relationship to the well-known cell proliferation marker Ki-67, which is detected only in dividing cells (in G_1, S, G_2, and M phase) and not in quiescent cells (in G_0 phase). Flow cytometry analysis showed that G_0M^{high}, G_0M^{low}, and part of G_0M^{neg} LT-HSCs were Ki-67 negative (Figure 1D). Mutually exclusive expression between G_0M and Ki-67 confirmed that G_0M was reliable as a marker for quiescent cells. G_0 cells are functionally defined as cells that spend more time before entry into their next cell cycle than G_1 cells (Foster et al., 2010). The time to the first cell division of G_0M^{high} and G_0M^{low} LT-HSCs in culture was about 35 h (Figure 1E). G_0M^{neg} LT-HSCs split into two subgroups: one with faster cell division and the other with slower cell division (Figure 1E). G_0M^{neg} LT-HSCs in the slower group showed similar time to the first cell division as G_0M^{high} and G_0M^{low} LT-HSCs, suggesting that these cells were also in G_0 phase. The time to the first cell division of G_0M^{neg} LT-HSCs in the faster group was about 15 h, the same as the time to the second cell division of G_0M^{high} LT-HSCs in culture, suggesting that the cells were in G_1/S/G_2/M phase, as cells in culture no longer go through G_0 phase after the first cell division (Figure 1E). These data indicate that G_0M^{high}, G_0M^{low}, and part of G_0M^{neg} LT-HSCs were functionally in G_0 phase and that G_0M started to degrade before G_0/G_1 transition *in vivo*.

The restriction point (R point) is defined as the point in G_1 phase of the mammalian cell cycle at which the cell becomes "committed" to enter the cell cycle and after which extracellular proliferation stimulants are no longer required (Cappell et al., 2016; Martinsson et al., 2005). We analyzed the relationship between the intensity of G_0M and the R point. Time-lapse live cell imaging showed that no G_0M^{pos} (G_0M^{high} and G_0M^{low}) LT-HSCs crossed the R point; in contrast, about half of G_0M^{neg} LT-HSCs crossed the R point (Figure S2F). The molecular basis for the R point has been proposed to be the hyper-phosphorylation of the tumor suppressor retinoblastoma protein (Rb)

Figure 1. Characterization of G_0M in HSCs

(A) Representative fluorescence-activated cell sorting (FACS) plots of G_0M expression in BM HSPCs in hG_0 mice (filled) or littermate control mice (unfilled) (left). Quantification of the mean fluorescence intensity (MFI) of G_0M normalized to MFI of littermate control cells in BM Lin$^-$c-Kit$^+$ cells (right; LT-HSC, ST-HSC, MPP2, and MPP3/4; n = 7 per group, seven independent experiments; CMP, GMP, and MEP: n = 3 per group, three independent experiments; one-way ANOVA).

(B) A representative FACS plot and gating strategy to separate G_0M^{high}, G_0M^{low}, and G_0M^{neg} populations in BM LT-HSCs.

(C) Frequencies of G_0M^{high}, G_0M^{low}, and G_0M^{neg} cells in BM HSPCs (n = 7 per group, seven independent experiments, one-way ANOVA).

(D) A representative FACS plot of Ki-67 and G_0M expression in BM LT-HSCs (left) and frequencies of Ki-67$^-$ cells in G_0M^{high}, G_0M^{low}, and G_0M^{neg} LT-HSCs (right; n = 4 per group, four independent experiments, one-way ANOVA).

(E) Time to first cell division of G_0M^{high} (n = 39), G_0M^{low} (n = 19), and G_0M^{neg} (n = 63) LT-HSCs and second cell division of G_0M^{high} LT-HSCs (n = 55) under condition of SCF 50 ng/mL, TPO 50 ng/mL, IL-3 10 ng/mL, IL-6 10 ng/mL, and EPO 4 U/mL (two independent experiments, one-way ANOVA).

(F) Chimerism of donor-derived cells in primary recipient mice transplanted with 100 donor LT-HSCs of indicated populations (left) and in secondary recipient mice transplanted with 5.0×10^6 whole BM cells of primary recipient mice (right; G_0M^{high}, n = 11; G_0M^{low}, n = 12; G_0M^{neg}, n = 11; three independent experiments, one-way ANOVA). Frequencies of successfully engrafted recipient mice are also shown.

(G) Lineage distribution of donor cells derived from G_0M^{high} and G_0M^{low} LT-HSCs (G_0M^{high}, n = 11; G_0M^{low}, n = 6; three independent experiments, Student's t test).

(H and I) The strategy for the BrdU label-retaining assay (left). Frequencies of BrdU$^+$ cells in G_0M^{high}, G_0M^{low}, and G_0M^{neg} LT-HSCs (H) after 2 weeks labeling *in vivo* and (I) on day 0, day 60, and day 90 relative to day 0 (day 0, n = 3; day 60, n = 7; day 90, n = 5; three independent experiments, one-way ANOVA).

For all panels, average, SEM is shown. *p < 0.05 and **p < 0.01. n.s., not significant.

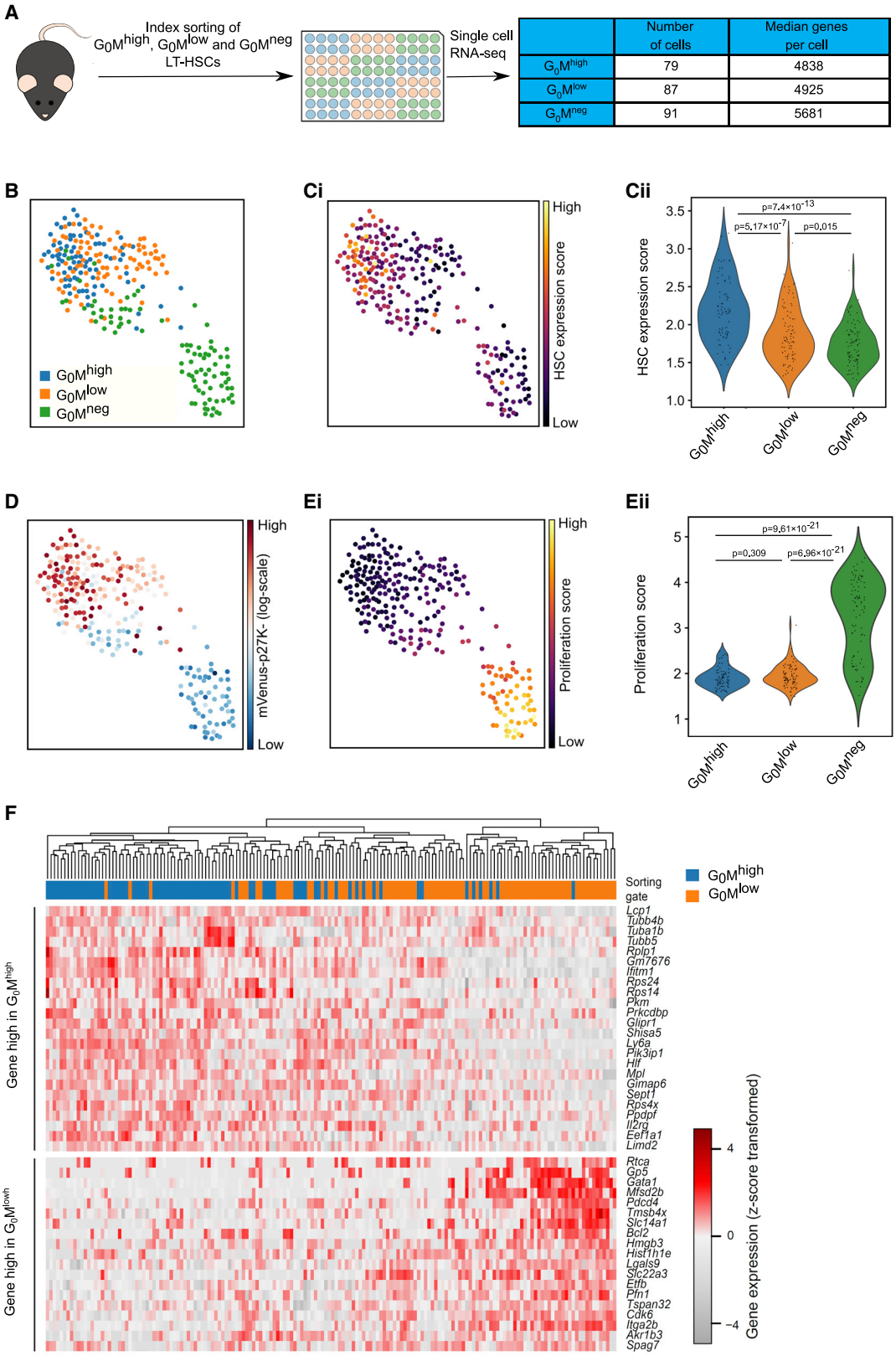

	Number of cells	Median genes per cell
G_0M^{high}	79	4838
G_0M^{low}	87	4925
G_0M^{neg}	91	5681

(legend on next page)

(Cappell et al., 2016; Martinsson et al., 2005). Rb was phosphorylated in G_0M^{neg} LT-HSCs but not in G_0M^{high} and G_0M^{low} LT-HSCs (Figure S2G). Thus, cells crossed the R point after becoming G_0M^{neg}. Collectively, these results suggest that G_0M accurately marks hematopoietic cells in G_0 phase *in vivo*.

G_0M Splits "True" HSCs into Two States: Dormant and Active

To examine how BM reconstitution potential is linked to cell cycle status, we transplanted 100 LT-HSCs from each fraction into lethally irradiated recipient mice. G_0M^{high} or G_0M^{low} LT-HSCs showed high or low BM reconstitution potential, respectively. In contrast, G_0M^{neg} LT-HSCs did not reconstitute the BM (Figure 1F). Secondary transplantations revealed that both G_0M^{high} and G_0M^{low} LT-HSCs, but not G_0M^{neg} LT-HSCs, exhibited BM reconstitution potential (Figure 1F), indicating that G_0M^{high} and G_0M^{low} LT-HSCs, but not G_0M^{neg} LT-HSCs, contained true HSCs. In fact, Kiel et al., 2005 showed that 47% of $CD150^+CD48^-$KSL cells (LT-HSCs) exhibit long-term multi-lineage reconstitution. Thus, half of LT-HSCs do not have HSC potential. No lineage bias between transplanted G_0M^{high} and G_0M^{low} LT-HSCs was observed (Figure 1G). G_0M^{high} LT-HSCs reconstituted in 9 of 11 mice, whereas G_0M^{low} cells reconstituted in 3 of 12 mice (Figure 1F), suggesting that the frequency of true HSCs in G_0M^{low} fraction was lower than that of G_0M^{high} fraction. These data indicate that both G_0M^{high} and G_0M^{low} cells contained true HSCs.

To further evaluate their dormancy, we performed a BrdU label-retaining assay, a method for detection of dormant cells in various tissues (Arai et al., 2004; Cotsarelis et al., 1990; Potten et al., 1978). After 2 weeks of BrdU treatment, 71.3% ± 2.3% of G_0M^{low} LT-HSCs were labeled, whereas only 39.4% ± 4.8% of G_0M^{high} LT-HSCs were labeled (Figure 1H). BrdU-labeled cells are reported to undergo about four or five cell divisions before BrdU expression becomes undetectable by flow cytometry (Wilson et al., 2008). Most G_0M^{high} LT-HSCs, but not G_0M^{low} LT-HSCs, retained BrdU for 90 days (Figure 1I), indicating that G_0M^{low} LT-HSCs are primed for cell division. Taken together, these results suggest that HSCs can be divided into dormant and active HSCs according to their G_0M intensity.

Gene Expression Analysis Identified True HSCs in G_0M^{high} and G_0M^{low} LT-HSCs

To further validate the properties of G_0M^{high}, G_0M^{low}, and G_0M^{neg} LT-HSCs, we performed single-cell RNA sequencing (scRNA-seq) analysis with index sorting (Figure 2A). Detection of fewer genes per cell and the lower mRNA content of $G_0M^{high/low}$ population compared with G_0M^{neg} LT-HSCs provided additional evidence that $G_0M^{high/low}$ cells were quiescent (Figures 2A and S3B). There was no correlation in expression profiles between G_0M and previously described HSC markers, such as Hoxb5, α-catulin, c-Myb, Fdg5, and Gprc5c (Figure S3C) (Acar et al., 2015; Cabezas-Wallscheid et al., 2017; Chen et al., 2016; Gazit et al., 2014; Sakamoto et al., 2015). The correlations between G_0M and these genes might not be detected because all these genes showed low RPKM (reads per kilobase of transcript per million mapped reads) values. The levels of p27 mRNA in G_0M^{high}, G_0M^{low}, and G_0M^{neg} LT-HSCs were comparable, indicating that expression of G_0M was not regulated at the mRNA level (Figure S3C). For visualization of the scRNA-seq data, we used a force-directed graph, a dimensionality reduction method that has previously been shown to be powerful at representing the structure within single-cell datasets (Weinreb et al., 2018). G_0M^{high} and G_0M^{low} LT-HSCs showed similar (overlap between orange and blue cells), whereas G_0M^{neg} LT-HSCs showed distinct pattern of gene expression (Figure 2B). We then examined the expression of a set of genes published as having high expression in true HSCs (MolO genes from Wilson et al., 2015). The cells with high expression of HSC-related genes were mostly within the G_0M^{high} fraction (Figures 2Ci and 2Cii). Next, we investigated the cell cycle status at the single-cell level. Visualizing G_0M levels from index data on the force-directed graph identified a clear gradient similar to the HSC expression score (Figure 2D). We then examined the expression of a set of cell cycle genes recently published by Ido Amit's group (Giladi et al., 2018), which highlighted a set of G_0M^{neg} LT-HSCs with high proliferation score (bottom right of force-directed graph) (Figures 2Ei and 2Eii). Thus, a major difference between $G_0M^{high/low}$ and G_0M^{neg} LT-HSCs was characterized by expression profiles of stem genes and proliferation genes (Figures 2B–2E), consistent with the fact that high HSC ability is correlated with low cell cycle activity (Giladi et al., 2018). To assess the difference between G_0M^{high} and G_0M^{low} LT-HSCs, we performed differential expression analysis (Wilcoxon rank-sum test, Benjamini-Hochberg correction for multiple testing) and identified 24 and 19 genes that are expressed significantly higher in G_0M^{high} and G_0M^{low} LT-HSCs, respectively (Figure 2F). Highly expressed genes in G_0M^{high} LT-HSCs include well-known HSC-related genes, such as *Hlf*, *Ifitm1*, *Mpl*, and *Ly6a*, confirming that this population contains true HSCs. On the other hand, highly expressed genes in G_0M^{low} LT-HSCs include genes associated with cell cycle or

Figure 2. scRNA-Seq of G_0M^{high}, G_0M^{low}, and G_0M^{neg} LT-HSCs

(A) Overview of single-cell RNA-seq experiment. Table provides a summary of the profiled cells after quality control.

(B) Force-directed graph visualization of single-cell profiles using the force atlas 2 algorithm. Each point represents a profiled cell and is colored by its G_0M sorting gate.

(C) Expression of a set of HSC marker genes from Wilson et al. (2015) was averaged within each cell to calculate the HSC expression score. This is displayed in force-directed graph (i) and in violin plots showing the score distribution for each G_0M sorting gate (ii). (Non-parametric Wilcoxon rank-sum test.)

(D) Force-directed graph colored by the levels of mVenus-$p27K^-$ reporter measured by index sorting.

(E) Expression of a set of cell cycle genes from Giladi et al. (2018) was averaged within each cell to calculate a proliferation for each score. This is displayed in force-directed graph (i) and in violin plots for each G_0M sorting gate (ii). (Non-parametric Wilcoxon rank-sum test.)

(F) Heatmap displaying expression of genes differentially expressed between G_0M^{high} and G_0M^{low} LT-HSCs. Expression for each gene was *Z* score transformed across the cells displayed in heatmap. G_0M sorting gate is displayed in color bar at the top of heatmap. Dendrogram indicates the result of hierarchical clustering on cells based on expression of genes in the heatmap.

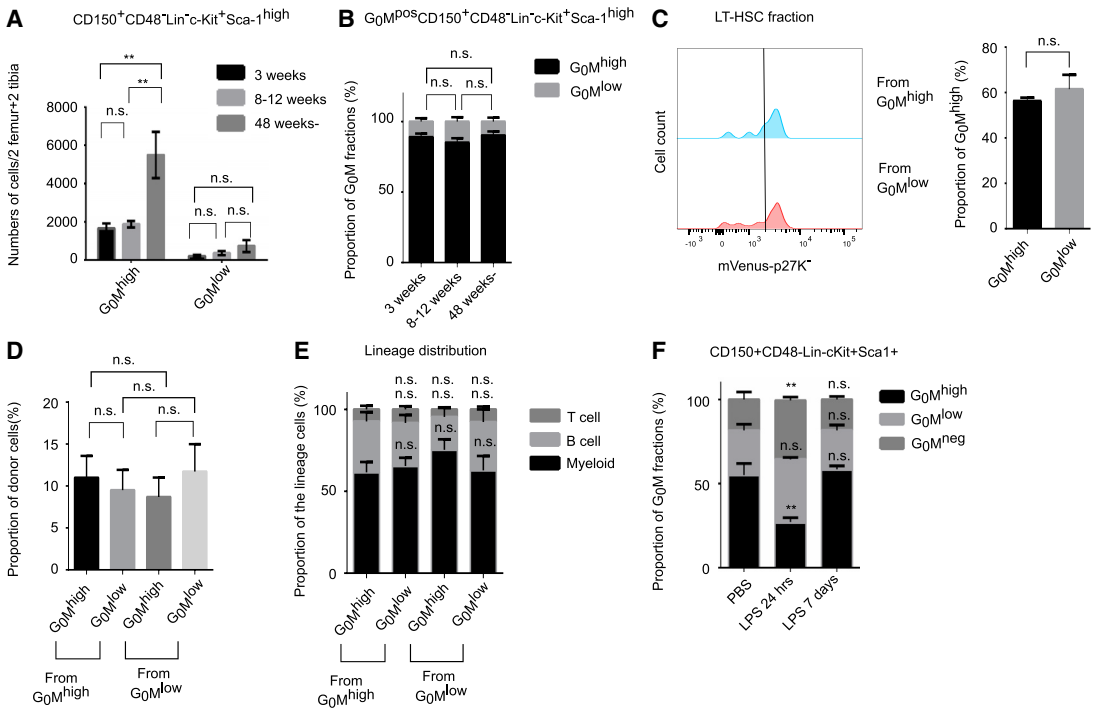

Figure 3. Kinetics Analysis of Dormant and Active HSCs

(A) The absolute number of G_0M^{high}/Sca-1^{high} or G_0M^{low}/Sca-1^{high} LT-HSCs of 3-week-old, 8- to 12-week-old, and 48-week-old hG_0 mice and littermate control mice (3 weeks old, n = 7; 8–12 weeks old, n = 5; 48 weeks old, n = 5 per genotype; three independent experiments, one-way ANOVA).

(B) Frequencies of G_0M^{high} and G_0M^{low} in G_0M^{pos}Sca-1^{high} LT-HSCs in 3-week-old, 8- to 12-week-old, and 48-week-old hG_0 mice (3 weeks old, n = 7; 8–12 weeks old, n = 5; 48 weeks old, n = 5 per genotypes; three independent experiments, one-way ANOVA).

(C) Representative FACS plots of G_0M expression (left) and frequencies of G_0M^{high} (right) in donor-derived LT-HSCs of primary recipient mice transplanted with G_0M^{high} or G_0M^{low} LT-HSCs at 16 weeks (G_0M^{high}, n = 9; G_0M^{low}, n = 3; three independent experiments, Student's t test).

(D) Chimerism of donor-derived cells in secondary recipient mice transplanted with 100 G_0M^{high} or G_0M^{low} LT-HSCs from primary recipient mice transplanted with 100 G_0M^{high} or G_0M^{low} LT-HSCs (G_0M^{high} from G_0M^{high}, n = 12; G_0M^{low} from G_0M^{high}, n = 12; G_0M^{high} from G_0M^{low}, n = 12; G_0M^{low} from G_0M^{low}, n = 11; two independent experiments, one-way ANOVA).

(E) Lineage distribution of donor cells derived from G_0M^{high} or G_0M^{low} LT-HSCs from primary recipient mice transplanted with 100 G_0M^{high} or G_0M^{low} LT-HSCs (G_0M^{high} from G_0M^{high}, n = 12; G_0M^{low} from G_0M^{high}, n = 12; G_0M^{high} from G_0M^{low}, n = 12; G_0M^{low} from G_0M^{low}, n = 11; two independent experiments, two-way ANOVA).

(F) Frequencies of G_0M^{high}, G_0M^{low}, and G_0M^{neg} in LT-HSCs 24 h after PBS or 24 h and 7 days after 5 mg/kg LPS intraperitoneal administration (PBS, n = 3; LPS 24 h, n = 4; LPS 7 days, n = 4; three or four independent samples, one-way ANOVA).

For all panels, average, SEM is shown. *p < 0.05 and **p < 0.01. n.s., not significant.

differentiation, such as *Gata1*, *Itga2b*, and *Cdk6*. Flow cytometry analysis also showed that high G_0M expression was correlated with expression patterns of HSC markers, such as c-Kit^{low}, Sca-1^{high}, $CD34^{neg}$, $CD41^{neg}$, and $EPCR^{high}$ (Balazs et al., 2006; Bernitz et al., 2016; Osawa et al., 1996; Shin et al., 2014; Wilson et al., 2015; Yamamoto et al., 2018) (Figure S3D).

Interestingly, some G_0M^{low} LT-HSCs expressed stem cell markers, including high Ly6a (Sca-1) (Figure 2F). A previous study reported that Sca-1^{high} is a marker of HSCs (Wilson et al., 2015), and our scRNA-seq data also showed that Sca-1 MFI was correlated with stem gene expression (Figure S3E). To address whether Sca-1^{high} cells in G_0M^{low} LT-HSCs were active HSCs, we examined their BM reconstitution potential and BrdU label-retaining capacity. Sca-1^{high} G_0M^{low} cells showed BM reconstitution potential (Figures S3F and S3G) but did not retain BrdU (Figures S3F and S3H). These data suggest that the G_0M^{low} fraction contains active HSCs.

Kinetics Analysis of Dormant and Active HSCs

To analyze kinetics of dormant and active HSCs at different ages, the numbers of G_0M^{high} and G_0M^{low} Sca-1^{high} HSCs were analyzed in 3-week-old, 8- to 12-week-old, and >1-year-old hG_0 mice. The number of true HSCs was calculated by limiting dilution transplantation assay. The number of dormant HSCs significantly increased after 1 year of age. The number of active HSCs also tended to increase with age (Figures 3A, S4A, and S4C). The ratio between dormant and active true HSCs remained unchanged over time (Figures 3B, S4B, and S4C). To analyze whether dormant and active states in HSCs were reversible, expression of G_0M was analyzed in BM LT-HSCs transplanted with G_0M^{high} or G_0M^{low} LT-HSCs. G_0M^{low} LT-HSCs were able to give rise to G_0M^{high} LT-HSCs after transplantation, and vice versa (Figure 3C). G_0M^{high} and G_0M^{low} LT-HSCs from either G_0M^{high} or G_0M^{low} LT-HSCs exhibited BM reconstitution potential (Figure 3D). No lineage bias between these transplanted fractions was observed

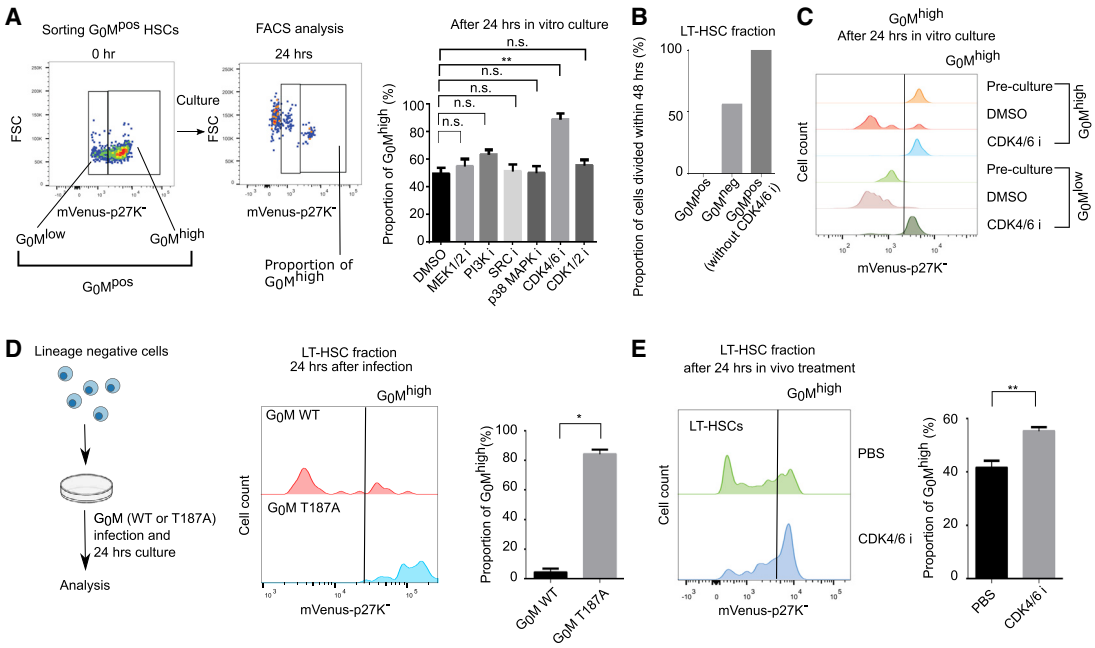

Figure 4. Inverse Correlation between the Intensity of G_0M and Cdk4/6 Activity

(A) Representative FACS plots of G_0M expression in LT-HSCs before and after 24 h culture under condition of SCF 50 ng/mL (left). Frequencies of G_0M^{high} cells treated with DMSO (n = 5), 20 μM MEK1/2 inhibitor (PD98059) (n = 3), 10 μM PI3K inhibitor (Ly294002) (n = 3), 20 μM p38MAPK inhibitor (SB203580) (n = 3), 5 μM SRC inhibitor (PP2) (n = 3), 1 μM CDK4/6 inhibitor (PD0332991) (n = 5), or 20 μM CDK1/2 inhibitor (roscovitine) (n = 3) for 24 h culture under condition of SCF 50 ng/mL (right; three to five independent experiments, one-way ANOVA).

(B) Frequencies of divided cells of G_0M^{pos} (n = 39) and G_0M^{neg} (n = 10) LT-HSCs under 1 μM CDK4/6 inhibitor (PD0332991) and G_0M^{pos} (n = 55) LT-HSCs under DMSO in 48 h culture (SCF 50 ng/mL, TPO 50 ng/mL, IL3 10 ng/mL, IL6 10 ng/mL, and EPO 4 U/mL).

(C) Representative FACS plots of G_0M expression of G_0M^{high} and G_0M^{low} LT-HSCs before and 24 h after culture under condition of DMSO or 1 μM CDK4/6 inhibitor (PD0332991).

(D) The strategy for the assay (left) and representative FACS plots of G_0M expression in LT-HSCs retrovirally transduced with G_0M (WT or T187A mutant) 24 h culture after transduction (middle). Frequencies of G_0M^{high} in LT-HSCs 24 h after G_0M (WT or T187A mutant) infection (right; n = 3 per group, three independent samples, Student's t test).

(E) Representative FACS plots of G_0M expression (left) and frequencies of G_0M^{high} (right) in LT-HSCs 24 h after PBS or 100 mg/kg CDK4/6 inhibitor (PD0332991) intraperitoneal administration (n = 6 per group, six independent samples, Student's t test).

For all panels, average, SEM is shown. *p < 0.05 and **p < 0.01. n.s., not significant.

(Figure 3E). These data indicate that the dormant and active states in HSCs were reversible. Next, we analyzed whether dormant and active states in HSCs were reversible or not in stress condition. The proportion of G_0M^{high} was decreased and that of G_0M^{neg} was increased 24 h after lipopolysaccharide (LPS) challenge and recovered to steady-state level 7 days after LPS challenge (Figure 3F). These data indicate that dormant HSCs are activated under stress conditions and recover after stress. Taken together, active true HSCs exist throughout the life and reversibly switch from dormant true HSCs under both steady-state and stress conditions.

Dormant and Active States of HSCs Were Defined by Cdk4/6 Activity

To investigate the regulators of dormant and active states in HSCs, we next analyzed molecular regulation of G_0M intensity. After 24 h in culture, most of the G_0M^{pos} LT-HSCs disappeared (Figure 4A). Studies have shown that phosphorylation and subsequent degradation of p27 are regulated by MEK, AKT, SRC, and CDK1/2 (Chu et al., 2008). To identify kinases that regulate p27 degradation in LT-HSCs, we cultured G_0M^{pos} LT-HSCs with inhibitors: PD98059 (MEK1/2 inhibitor), Ly294002 (PI3K inhibitor), SB203580 (p38 MAPK inhibitor), PP2 (SRC inhibitor), PD0332991 (CDK4/6 inhibitor), and roscovitine (CDK1/2 inhibitor). Among these inhibitors, PD0332991 most efficiently inhibited degradation of p27 (Figure 4A), consistent with previous reports that both Cdk4/6 and their partner cyclinD1/2/3 are indispensable for cell division of hematopoietic cells (Kozar et al., 2004; Malumbres et al., 2004). Time-lapse live cell imaging of G_0M^{pos} and G_0M^{neg} LT-HSCs with or without CDK4/6 inhibitor in culture showed that G_0M^{pos} LT-HSCs never divided in the presence of CDK4/6 inhibitor, whereas half of G_0M^{neg} LT-HSCs did in 48 h (Figure 4B). Moreover, CDK4/6 inhibitor reverted G_0M^{low} LT-HSCs to G_0M^{high} LT-HSCs without cell division (Figures 4B and 4C). We also found that G_0M degradation depended on phosphorylation at threonine 187 of p27, a known target of Cdks (Montagnoli et al., 1999) (Figure 4D). Thus, these data suggest that G_0M intensity is controlled by Cdk4/6-induced p27 phosphorylation at threonine 187. The different intensity of G_0M between G_0M^{high} and G_0M^{low} LT-HSCs probably reflects

A

	G_0M^{high}		$G_0Mmarker^{low}$		G_0M^{neg}	
	G_0M^{high}-1	G_0M^{high}-2	G_0M^{low}-1	G_0M^{low}-2	G_0M^{neg}-1	G_0M^{neg}-2
PSM	6066	5734	7375	7118	12157	11807
Unique peptide	4916	4649	6042	5744	9945	9579
Protein	1321	1260	1436	1366	1985	1900
	1492		1621		2222	
	2389					

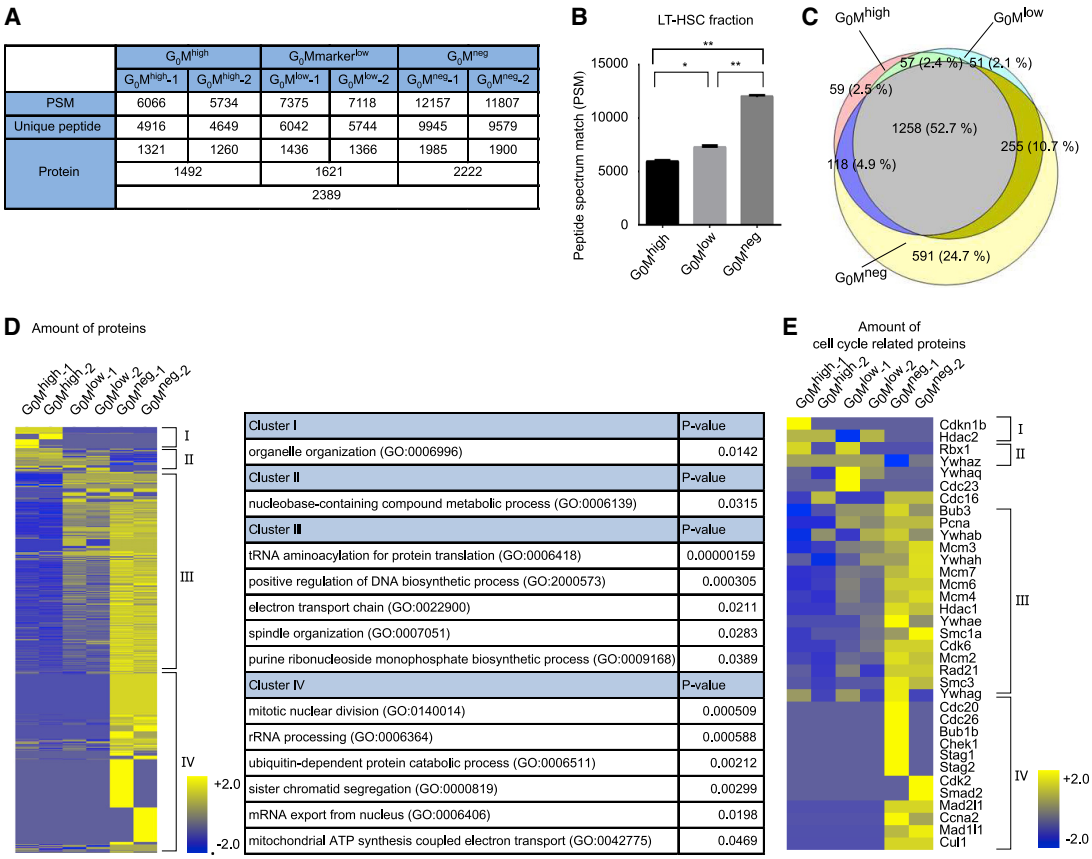

Cluster I	P-value
organelle organization (GO:0006996)	0.0142
Cluster II	**P-value**
nucleobase-containing compound metabolic process (GO:0006139)	0.0315
Cluster III	**P-value**
tRNA aminoacylation for protein translation (GO:0006418)	0.00000159
positive regulation of DNA biosynthetic process (GO:2000573)	0.000305
electron transport chain (GO:0022900)	0.0211
spindle organization (GO:0007051)	0.0283
purine ribonucleoside monophosphate biosynthetic process (GO:0009168)	0.0389
Cluster IV	**P-value**
mitotic nuclear division (GO:0140014)	0.000509
rRNA processing (GO:0006364)	0.000588
ubiquitin-dependent protein catabolic process (GO:0006511)	0.00212
sister chromatid segregation (GO:0000819)	0.00299
mRNA export from nucleus (GO:0006406)	0.0198
mitochondrial ATP synthesis coupled electron transport (GO:0042775)	0.0469

Figure 5. Proteomics Analysis of G_0M^{high}, G_0M^{low} and G_0M^{neg} LT-HSCs

(A) Peptide spectrum match (PSM), the number of identified peptides, and the number of identified proteins in G_0M^{high}, G_0M^{low}, and G_0M^{neg} LT-HSCs by mass analysis.

(B) The number of peptide spectrum matches (PSMs) detected by mass analysis (n = 2 per group, technical duplicate). *p < 0.05 and **p < 0.01, one-way ANOVA.

(C) Venn diagram of proteins identified in G_0M^{high}, G_0M^{low}, and G_0M^{neg} LT-HSCs by mass analysis.

(D) Differentially enriched proteins among G_0M^{high}, G_0M^{low}, and G_0M^{neg} LT-HSCs by mass analysis. Heatmap representing the number of PSMs of the proteins. The number of PSMs of the proteins was displayed by *Z* score transformation across the sample in heatmap (left; n = 2 per group, technical duplicate). The proteins are divided into four subgroups by enrichment pattern. Table displaying Gene Ontology terms enriched in each subgroup and p values (right).

(E) Heatmap displaying expression of cell cycle proteins from KEGG pathway. Expression for each protein was displayed by *Z* score transformation across the samples in heatmap (n = 2 per group, technical duplicate).

the difference in Cdk4/6 activity. To examine the role of Cdk4/6 in the regulation of HSC dormancy *in vivo*, we injected CDK4/6 inhibitor or PBS into hG_0 mice and assessed the intensity of G_0M in LT-HSCs 24 h after injection. Consistent with the *in vitro* data, CDK4/6 inhibitor increased the proportion of G_0M^{high} LT-HSCs (Figure 4E) *in vivo*. Together, G_0M^{low} LT-HSCs exhibited higher Cdk4/6 activity than G_0M^{high} LT-HSCs.

To further evaluate molecular differences between G_0M^{high}, G_0M^{low}, and G_0M^{neg} LT-HSCs, the proteins of these cells were digested and analyzed using liquid chromatography-tandem mass spectrometry (LC-MS/MS). The number of identified spectra, called peptide spectrum match (PSM), and the number of identified proteins in samples also provided evidence supporting that $G_0M^{high/low}$ LT-HSCs were quiescent (Figures 5A–5C). Proteins are listed with characteristic dynamics, highly expressed in G_0M^{high} (cluster I), gradually downregulated as G_0M intensity decreased (cluster II), gradually upregulated as G_0M intensity decreased (cluster III), and highly expressed in G_0M^{neg} cells (cluster IV) (Figure 5D). Gene Ontology term analysis showed that cell cycle proteins were enriched in cluster III and cluster IV (Figure 5D). Cell cycle genes in the KEGG pathway were extracted from these clusters (Figure 5E). Cluster IV contained cyclin A, Cdk2, and Cdc20, which are important for S/G_2/M progression (Figure 5E). As expected, cluster III contains Cdk6, expression of which defines active HSCs, as previously described, supporting the conclusion that G_0M^{low} LT-HSCs are active HSCs (Cabezas-Wallscheid et al., 2017). Moreover, cluster III contained the pre-replication complex (Mcm and Pcma) and the cohesin complex (Smc and Rad21), indicating that cell cycle activation is primed in G_0M^{low} LT-HSCs (Figure 5E). Thus, cell cycle proteins, especially Cdk6, were upregulated in G_0M^{low} LT-HSCs. Taken together, these data suggest that one of the key molecular differences between dormant and active states of HSCs is Cdk4/6 activity.

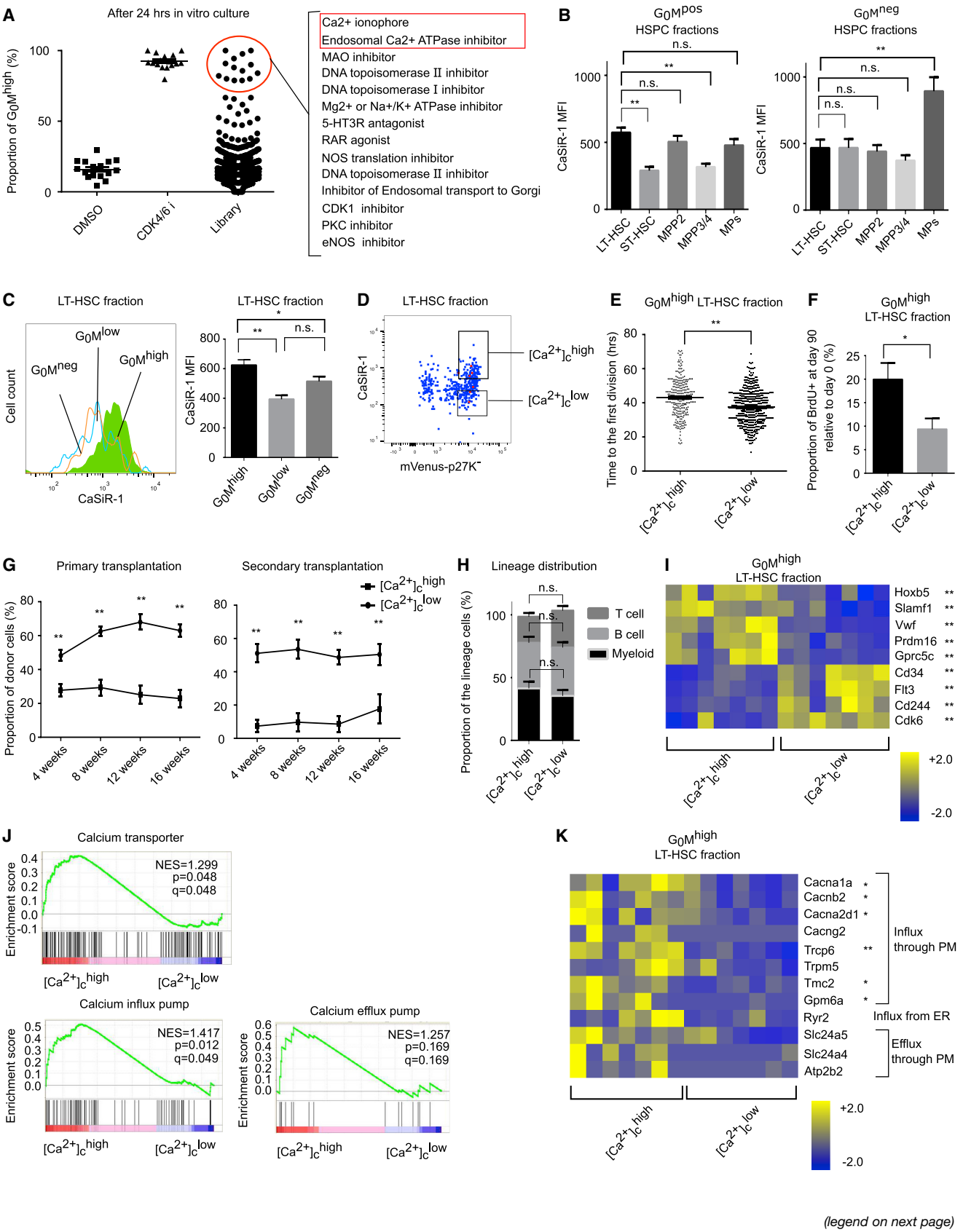

(legend on next page)

High $[Ca^{2+}]_c$ Is Linked to Dormancy of HSCs

To identify the machinery underlying HSC quiescence, we used an inhibitor library containing 1,280 validated inhibitors. The proportion of G_0M^{high} cells was measured after 24 h culture of sorted G_0M^{pos} LT-HSCs with each inhibitor in the library. Fourteen inhibitors kept the G_0M expression high after 24 h culture, similar to the Cdk4/6 inhibitor. Interestingly, 2 of the 14 inhibitors (thapsigargin and calcimycin) were calcium regulators (Figures 6A and S5A). Both thapsigargin and calcimycin are known to increase $[Ca^{2+}]_c$. Thapsigargin is a sarco/endoplasmic reticulum calcium-ATPase (SERCA) inhibitor, which increases $[Ca^{2+}]_c$ by leaking calcium from endoplasmic reticulum (ER). Calcimycin is a calcium ionophore, which increases $[Ca^{2+}]_c$ by binding to calcium and transporting it through the plasma membrane. To clarify the role of $[Ca^{2+}]_c$ in HSCs, $[Ca^{2+}]_c$ was measured in BM HSPCs. LT-HSCs showed higher $[Ca^{2+}]_c$ than ST-HSCs and MPP3/4s in quiescent cells (G_0M^{pos} cells) (Figure 6B). Moreover, G_0M^{high} LT-HSCs showed higher $[Ca^{2+}]_c$ than G_0M^{low} LT-HSCs (Figures 6C and S5B), indicating the heterogeneity of $[Ca^{2+}]_c$ in HSCs, as described previously (Luchsinger et al., 2016). Consistent with this, $[Ca^{2+}]_c^{high}$ and $[Ca^{2+}]_c^{low}$ cells were present among G_0M^{high} LT-HSCs (hereafter referred to $[Ca^{2+}]_c^{high}$ cells and $[Ca^{2+}]_c^{low}$ cells) (Figure 6D). Therefore, we compared the functions of these two types of LT-HSCs. The time to the first division of $[Ca^{2+}]_c^{high}$ cells was longer and *in vivo* division frequencies of $[Ca^{2+}]_c^{high}$ cells were lower than those of $[Ca^{2+}]_c^{low}$ cells (Figures 6E and 6F). Moreover, $[Ca^{2+}]_c^{high}$ cells showed higher BM reconstitution potential than $[Ca^{2+}]_c^{low}$ cells (Figure 6G). No lineage bias was observed between $[Ca^{2+}]_c^{high}$ and $[Ca^{2+}]_c^{low}$ cells (Figure 6H). To further understand their hierarchy, we examined whether $[Ca^{2+}]_c^{high}$ cells can give rise to $[Ca^{2+}]_c^{low}$ cells, and vice versa. We analyzed $[Ca^{2+}]_c$ of G_0M^{high} LT-HSCs from the recipient mice reconstituted by either $[Ca^{2+}]_c^{high}$ or $[Ca^{2+}]_c^{low}$ cells 4 months after transplantation. $[Ca^{2+}]_c^{high}$ cells were able to give rise to $[Ca^{2+}]_c^{low}$ cells, and vice versa (Figure S5C). $[Ca^{2+}]_c^{high}$ and $[Ca^{2+}]_c^{low}$ cells from the first recipients reconstituted by either $[Ca^{2+}]_c^{high}$ or $[Ca^{2+}]_c^{low}$ cells had BM reconstitution potential in the secondary recipients (Figure S5D). Intriguingly, recent studies showed that increasing $[Ca^{2+}]_c$ of HSCs is important for cell cycle activation of HSCs under stress conditions induced by 5-fluorouracil (5FU) and cytokines (Sugimura et al., 2012; Umemoto et al., 2018). Therefore, we measured $[Ca^{2+}]_c$ of G_0M^{high} LT-HSCs in an LPS-induced stress model. LPS augmented $[Ca^{2+}]_c$ of G_0M^{high} LT-HSCs (Figure S5E), implying that cycling cells possess high $[Ca^{2+}]_c$. Consistent with this, $[Ca^{2+}]_c$ of G_0M^{neg} MPs (cycling cells) was much higher than that of G_0M^{high} LT-HSCs in steady-state condition (Figure 6B). Together, $[Ca^{2+}]_c^{high}$ HSCs are most dormant and have the highest BM reconstitution ability among LT-HSCs, but their $[Ca^{2+}]_c$ was lower than that of cycling cells.

To clarify molecular difference between $[Ca^{2+}]_c^{high}$ and $[Ca^{2+}]_c^{low}$ cells, we performed RNA-seq analysis using $[Ca^{2+}]_c^{high}$ and $[Ca^{2+}]_c^{low}$ cells. Principal-component analysis (PCA) and hierarchical clustering showed that $[Ca^{2+}]_c^{high}$ and $[Ca^{2+}]_c^{low}$ cells were distinct (Figures S5F and S5G). $[Ca^{2+}]_c^{high}$ and $[Ca^{2+}]_c^{low}$ cells were not fully separated in PCA, indicating that there were not huge differences between these populations (Figure S5F). Consistent with the functional assay, HSC-related genes, such as Hoxb5, Slamf1, Vwf, and Prdm16 (Aguilo et al., 2011; Chen et al., 2016; Kiel et al., 2005), were highly expressed in $[Ca^{2+}]_c^{high}$ cells (Figure 6I). In contrast, progenitor-related genes, such as CD34, Flt3, and CD244 (Adolfsson et al., 2001; Oguro et al., 2013; Osawa et al., 1996), were highly expressed in $[Ca^{2+}]_c^{low}$ cells (Figure 6I). Moreover, $[Ca^{2+}]_c^{high}$ cells showed high expression of Gprc5c, which is highly expressed in dormant HSCs (Cabezas-Wallscheid et al., 2017; Scheicher et al., 2015), while $[Ca^{2+}]_c^{low}$ cells expressed high levels of Cdk6 (Figure 6I). Calcium transporter genes, especially influx channels, were also highly expressed in $[Ca^{2+}]_c^{high}$ cells (Figures 6J and 6K), suggesting that high expression of calcium influx channels results in high $[Ca^{2+}]_c$ in $[Ca^{2+}]_c^{high}$ cells. These data suggest that $[Ca^{2+}]_c^{high}$ cells are more dormant and have higher BM reconstitution potential than $[Ca^{2+}]_c^{low}$ cells in G_0M^{high} LT-HSCs.

Figure 6. Dormant HSCs Exhibit High $[Ca^{2+}]_c$

(A) G_0M^{pos} LT-HSCs were treated with DMSO, 1 μM CDK4/6 inhibitor (PD0332991), or 3 μM chemicals in small chemical library for 24 h culture under condition of SCF 50 ng/mL and TPO 50 ng/mL. Frequencies of G_0M^{high} cells after 24 h culture are shown (DMSO, n = 18; CDK4/6 inhibitor, n = 18; small chemical library, n = 1,280; nine independent experiments).

(B) Quantification of the MFI of CaSiR-1 in G_0M^{pos} (left)/G_0M^{neg} (right) LT-HSC, ST-HSC, MPP2, MPP3/4, and MP fractions (n = 10 per group, seven independent experiments, one-way ANOVA).

(C) Representative FACS plots (left) and quantification of the MFI of CaSiR-1 (right) of G_0M^{high}, G_0M^{low}, and G_0M^{neg} LT-HSCs (n = 10 per group, seven independent experiments, one-way ANOVA).

(D) Representative FACS plots and gating strategy to separate $[Ca^{2+}]_c^{high}$ and $[Ca^{2+}]_c^{low}$ populations in LT-HSCs.

(E) Time to the first cell division of $[Ca^{2+}]_c^{high}$ and $[Ca^{2+}]_c^{low}$ cells in culture under condition of SCF 50 ng/mL and TPO 50 ng/mL with DMSO ($[Ca^{2+}]_c^{high}$, n = 277; $[Ca^{2+}]_c^{low}$, n = 459; three independent experiments, Student's t test).

(F) Frequencies of $BrdU^+$ cell fractions in $[Ca^{2+}]_c^{high}$ and $[Ca^{2+}]_c^{low}$ cells on day 90 relative to day 0 (n = 6 per group, six independent samples, Student's t test).

(G) Chimerism of donor-derived cells in primary recipient mice transplanted with 100 donor $[Ca^{2+}]_c^{high}$ or $[Ca^{2+}]_c^{low}$ cells (left) and secondary recipient mice transplanted with 5.0×10^6 whole BM cells from primary recipient mice (right; n = 12 per group, two independent experiments, Student's t test).

(H) Lineage distribution of donor cells derived from $[Ca^{2+}]_c^{high}$ or $[Ca^{2+}]_c^{low}$ cells (n = 12 per group, two independent experiments, Student's t test).

(I) Heatmap of the expression of HSC-related genes and progenitor-related genes in $[Ca^{2+}]_c^{high}$ and $[Ca^{2+}]_c^{low}$ cells. Expression for each mRNA was displayed by *Z* score transformation across the samples in heatmap (n = 7 per group, two independent experiments, Student's t test).

(J) Enrichment of calcium transporter genes between $[Ca^{2+}]_c^{high}$ and $[Ca^{2+}]_c^{low}$ cells. NES, normalized enrichment score; q value, false discovery rate.

(K) Heatmap of the expression of calcium transporter genes in $[Ca^{2+}]_c^{high}$ and $[Ca^{2+}]_c^{low}$ cells. Expression for each mRNA was displayed by *Z* score transformation across the sample in heatmap (n = 7 per group, two independent experiments, Student's t test). PM, plasma membrane. ER, endoplasmic reticulum.

For all panels, average, SEM is shown. *$p < 0.05$ and **$p < 0.01$. n.s., not significant.

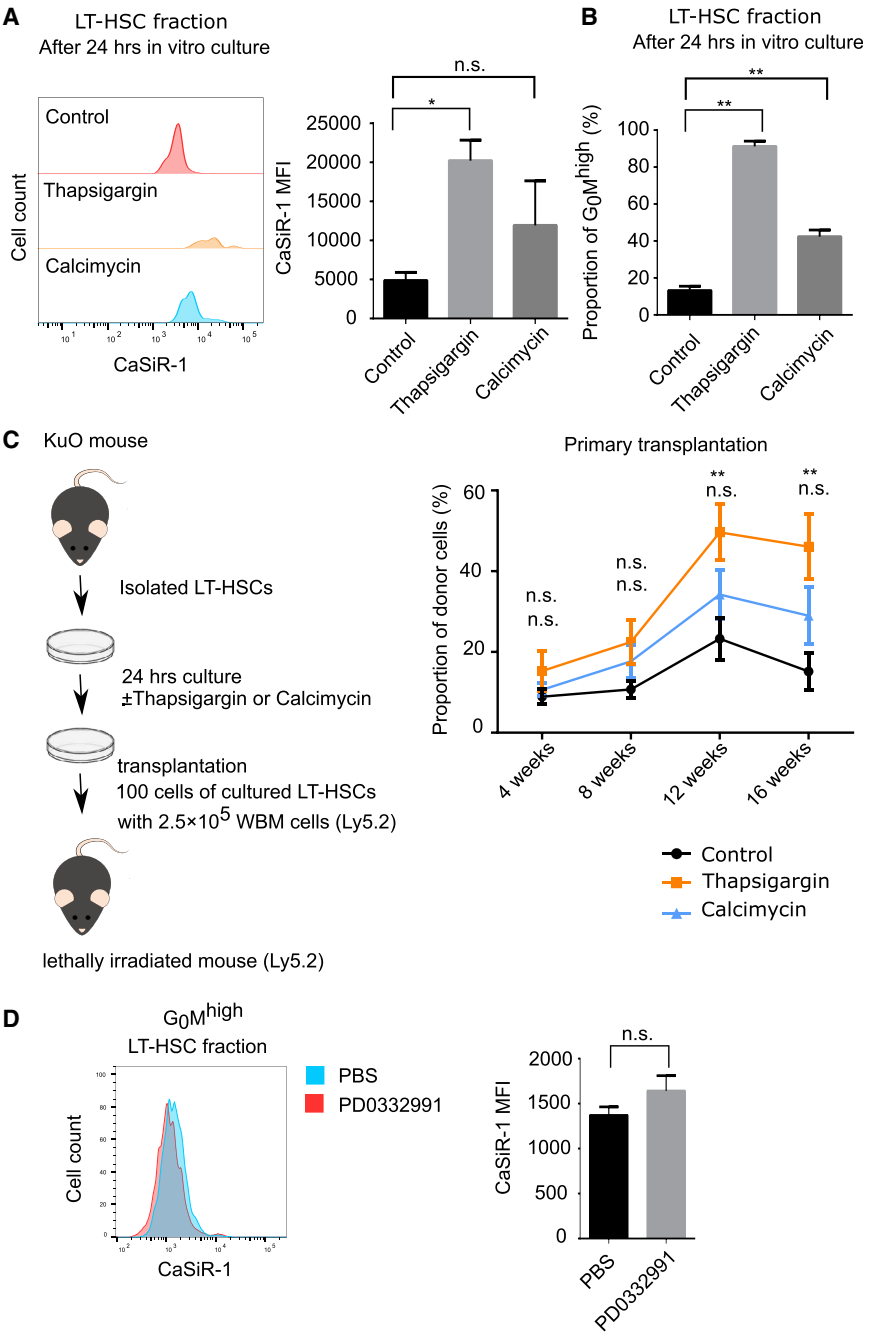

Figure 7. Upregulation of $[Ca^{2+}]_c$ Enhances Dormancy of HSCs

(A) Representative FACS plots of CaSiR-1 (left) and the MFI of CaSiR-1 (right) treated with DMSO (n = 4), 0.1 μM thapsigargin (n = 4), or 1 μM calcimycin (n = 4) for 24 h culture under condition of SCF 50 ng/mL and TPO 50 ng/mL (three independent experiments, one-way ANOVA).

(B) Frequencies of G_0M^{high} cells treated with DMSO (n = 7), 0.1 μM thapsigargin (n = 6), or 1 μM calcimycin (n = 7) for 24 h culture under condition of SCF 50 ng/mL and TPO 50 ng/mL (six or seven independent experiments, one-way ANOVA).

(C) The strategy for the transplantation assay (left) and chimerism of donor-derived cells in primary recipient mice transplanted with 100 donor LT-HSCs 24 h after culture with DMSO, thapsigargin, or calcimycin (right; DMSO, n = 12; thapsigargin, n = 11; calcimycin, n = 13; two independent experiments, one-way ANOVA).

(D) Representative FACS histograms (left) and quantification of the MFI of CaSiR-1 (right) of G_0M^{high} LT-HSCs 24 h after PBS or 100 mg/kg CDK4/6 inhibitor (PD0332991) intraperitoneal administration (n = 6 per group, six independent samples, Student's t test).

For all panels, average, SEM is shown. *p < 0.05 and **p < 0.01. n.s., not significant.

Upregulation of $[Ca^{2+}]_c$ in HSCs Enhances Dormancy of HSCs

To examine the relation between $[Ca^{2+}]_c$ and HSC dormancy, we assessed the effects of $[Ca^{2+}]_c$ modulation in HSCs using thapsigargin and calcimycin to increase $[Ca^{2+}]_c$ or verapamil to decrease $[Ca^{2+}]_c$. Thapsigargin strongly increased $[Ca^{2+}]_c$ and inhibited G_0M degradation without cell division in LT-HSCs (Figures 7A, 7B, and S6A). Moreover, upregulation of $[Ca^{2+}]_c$ by thapsigargin increased BM reconstitution potential of LT-HSCs (Figure 7C). Calcimycin also showed similar but weaker effects on HSCs. These data suggest that upregulation of $[Ca^{2+}]_c$ inhibits cell cycle progression of LT-HSCs and enhances their BM reconstitution potential. Thus, upregulation of $[Ca^{2+}]_c$ is important for dormancy of HSCs, consistent with the idea that high HSC ability is correlated with low cell cycle activity (Giladi et al., 2018). In contrast, verapamil decreased $[Ca^{2+}]_c$ in LT-HSCs, but unexpectedly did not show any effects on reconstitution potential of $[Ca^{2+}]_c^{high}$ and $[Ca^{2+}]_c^{low}$ cells (Figures S6B and S6C). Finally, we examined whether induction of dormancy increases $[Ca^{2+}]_c$. Treatment with a CDK4/6 inhibitor, which keeps HSCs dormant, did not change $[Ca^{2+}]_c$ in G_0M^{high} LT-HSCs (Figure 7D). Collectively, these data indicate that high $[Ca^{2+}]_c$ is important for dormancy of HSCs, but quiescence itself does not increase $[Ca^{2+}]_c$ in steady-state condition.

DISCUSSION

Previously, dormant and active HSCs were detected using label-retaining and DNA barcoding assays (Bernitz et al., 2016; Cabezas-Wallscheid et al., 2017; Rodriguez-Fraticelli et al., 2018; Sun et al., 2014; van der Wath et al., 2009). These studies have

revealed the mechanisms defining the dormant and active states of HSCs, which are important for understanding regulation of HSC self-renewal and differentiation. However, these methods are not suitable for detection of active HSCs in young mice, as they require long-term chasing. On the other hand, G_0M presented here could be used to distinguish active LT-HSCs (G_0M^{low}) from dormant LT-HSCs (G_0M^{high}) at any given time (Figures 1, 2, and 3) without long-term chasing. Thus, G_0M enabled us to analyze kinetics and molecular regulation of dormant and active LT-HSCs over the lifespan.

Although it is thought that active somatic stem cells reversibly switch to dormant state after regeneration (Buczacki et al., 2013; Li and Clevers, 2010; Wilson et al., 2008), there has been no direct evidence showing switching between active and dormant HSC states. Previously studies could not examine whether active HSCs can switch to dormant ones, and vice versa, because of the requirement for long-term chasing (GFP^{Lo} cells in H2B-GFP chasing model). In this study, we showed that G_0M^{low} LT-HSCs can revert to G_0M^{high} LT-HSCs in recipient mice (Figures 3C and 3D). Thus, our data provide evidence demonstrating that active LT-HSCs can revert to the dormant state *in vivo*.

The long-term label-retaining cell (LRC) assay showed that about half of G_0M^{high} LT-HSCs retained BrdU for 90 days. On the other hand, few G_0M^{low} LT-HSCs retained BrdU after the same time span (Figure 1I). These observations indicate that half of G_0M^{high} LT-HSCs correspond to previously reported ''stable label-retaining HSCs'' (sLR-HSCs), while the remaining G_0M^{high} LT-HSCs could proceed to active LT-HSCs or differentiate to mature blood cells.

The number of HSCs is increased after 1 year of mouse age (Beerman et al., 2010; Benz et al., 2012; Bernitz et al., 2016; Dykstra et al., 2011; Ema et al., 2000; Rossi et al., 2005; Yamamoto et al., 2018). It was reported that sLR-HSCs underwent symmetrical cell division about four times in the lifespan and committed to progenitors and differentiated cells when required (Bernitz et al., 2016), and the cell cycle status of HSCs was not active throughout the lifespan (Noda et al., 2009). Consistent with these observations, the number of G_0M-defined dormant LT-HSCs (half of them were sLR-HSCs) unchanged until 12 weeks of age and increased about 2-fold at 1 year of age (Figure 3A). On the other hand, changes in number of active HSCs across the lifespan have not been reported. Here we showed that the number of active HSCs also tended to increase, and the ratio between dormant and active HSCs was unchanged over the age (Figure 3B). These observations suggest that active HSCs undergo both self-renewal and differentiation division. Given that active HSCs can give rise to dormant ones, an increase of dormant HSCs with age could be due to not only self-renewal of dormant HSCs but also a supply from active HSCs.

Our proteomics analysis showed that several cell cycle proteins were already upregulated in active HSCs (Figure 5D). In particular, transcriptome and proteome analysis showed that both Cdk6 mRNA and protein increased in active HSCs (Figures 2F and 5E), consistent with the previous reports (Cabezas-Wallscheid et al., 2017; Laurenti et al., 2015). Moreover, we showed that both the amount of Cdk6 mRNA and protein and Cdk4/6 activity are inversely correlated with dormancy of HSCs, as G_0M is a substrate of Cdk4/6 and thus can monitor Cdk4/6 activity (Figures 4 and 5). Thus, the dormant and active states of LT-HSCs can be defined by Cdk4/6 activity.

We showed here that high $[Ca^{2+}]_c$ in LT-HSCs was linked to their dormancy in steady-state condition. Luchsinger et al. (2016) also showed that $[Ca^{2+}]_c$ is higher in $CD150^{high}$ HSCs than $CD150^{low}$ HSCs in steady-state condition, similar to our data showing that $[Ca^{2+}]_c$ of G_0M^{high} LT-HSCs was higher than that of G_0M^{low} LT-HSCs. These observations indicate the heterogeneity of $[Ca^{2+}]_c$ in HSCs. However, the same group also showed that $[Ca^{2+}]_c$ of HSCs was lower than that of MPPs in steady-state condition and that $[Ca^{2+}]_c^{high}$ HSCs showed enhanced long-term repopulation compared with $[Ca^{2+}]_c^{low}$ HSCs (Luchsinger et al., 2019). Intriguingly, the conclusions from their transplantation data were not consistent with our data. A possible explanation for this discrepancy is the difference in target populations. Our target populations are G_0M-defined dormant HSCs, whereas their populations are conventional HSCs, which correspond to our G_0M^{high}, G_0M^{low}, and G_0M^{neg} LT-HSCs. $[Ca^{2+}]_c^{high}$ cells accounted for 19.1% ± 1.0% of conventional HSCs. Of note, $[Ca^{2+}]_c$ of G_0M^{neg} LT-HSCs was also high (Figure 6D). Therefore, $[Ca^{2+}]_c^{high}$ conventional HSCs should contain G_0M^{neg} LT-HSCs, which show no reconstitution potential, resulting in the dilution of long-term reconstitution potential of $[Ca^{2+}]_c^{high}$ conventional HSCs. On the other hand, $[Ca^{2+}]_c^{low}$ conventional HSCs should contain G_0M^{high} and G_0M^{low} LT-HSCs and few G_0M^{neg} LT-HSCs, resulting in higher reconstitution potential. Other groups showed that HSCs undergo cell division as a consequence of increased $[Ca^{2+}]_c$ (Sugimura et al., 2012; Umemoto et al., 2018). These data showed that increasing $[Ca^{2+}]_c$ of HSCs is important for cell cycle activation of HSCs in stress conditions induced by 5FU and cytokines, but not in steady-state condition. In fact, we also showed that $[Ca^{2+}]_c$ of dormant HSCs increased in the LPS-induced stress condition (Figure S5E). Therefore, high $[Ca^{2+}]_c$ could have different functions at different cell cycle phases. High $[Ca^{2+}]_c$ activates HSCs to proliferate in the cycling phase, whereas high $[Ca^{2+}]_c$ keeps HSCs dormant in the quiescent phase (Figures 6E and 6F).

In the present study, we have shown that upregulation of $[Ca^{2+}]_c$ by thapsigargin inhibited cell cycle progression of dormant HSCs and enhanced their BM reconstitution potential (Figures 7A–7C). These observations indicated that high $[Ca^{2+}]_c$ is linked to dormancy. On the other hand, a Cdk4/6 inhibitor, which keeps cells quiescent, did not increase $[Ca^{2+}]_c$. Collectively, upregulation of $[Ca^{2+}]_c$ enhances quiescence of HSCs, but induction of quiescence does not affect $[Ca^{2+}]_c$ of HSCs in steady-state condition.

G_0M is a biomarker that enables high-throughput screening of small-molecule compounds as candidate regulators of HSC states. The present small-molecule screening also detected the agonist for retinoic acid signaling, a crucial regulator of HSC dormancy (Cabezas-Wallscheid et al., 2017). Thus, other signaling pathways detected in our screening are attractive targets to further understand stem cell dormancy.

Collectively, our findings open up avenues for future research addressing the mechanisms that regulate the dormant and active states. Importantly, the G_0M mouse may be broadly applicable to other adult tissue stem cell systems, as well as cancer stem cells,

in the identification of drugs that can specifically target cells in G_0 that escape many of the current cancer treatments.

STAR★METHODS

Detailed methods are provided in the online version of this paper and include the following:

- KEY RESOURCES TABLE
- LEAD CONTACT AND MATERIALS AVAILABILITY
- EXPERIMENTAL MODEL AND SUBJECT DETAILS
  - Mice
  - Cell lines
- METHOD DETAILS
  - Antibodies, Flow Cytometry and Cell Purification
  - BrdU Treatment and Label-Retaining Assays
  - Calcium Measurement
  - *In vivo* Treatment
  - Bone Marrow Transplantation
  - HSC Culture
  - Viral Transduction
  - Time-lapse Live-cell Imaging of LT-HSC
  - Single-cell RNA-Seq
  - RNA-Seq
  - Proteomic Analysis
- QUANTIFICATION AND STATISTICAL ANALYSIS
- DATA AND CODE AVAILABILITY

SUPPLEMENTAL INFORMATION

Supplemental Information can be found online at https://doi.org/10.1016/j.celrep.2019.11.061.

ACKNOWLEDGMENTS

We thank Ryoko Koitabashi for performing RNA-seq and the Drug Discovery Initiative at the University of Tokyo for providing the chemical library. We acknowledge the IMSUT FACS Core Laboratory, the IMSUT Imaging Core Laboratory, and the IMSUT Animal Research Center. This project is supported by medical research grants (fundamental research) from the Takeda Science Foundation to Y.T. and research grants from the Tokyo Biochemical Research Foundation (TBRF) to Y.T.

AUTHOR CONTRIBUTIONS

T. Fukushima and Y.T. designed and performed most of the experiments. F.K.H. analyzed the scRNA-seq data. T.U. and H.T. analyzed the RNA-seq data. K.T. assisted with calcium measurement. S.A., Y.H., T. Fujino, R.T., T.Y., and K.C.K. assisted with cell culture. C.-H.C. and Y.I. performed proteomics experiments. H.H. generated the G_0M mouse line. T. Fukushima, Y.T., S.A., S.G., B.G., and T.K. wrote the manuscript. T.K., S.G., T. Fukuyama, and B.G. supervised and coordinated the project.

DECLARATION OF INTERESTS

The authors declare no competing interests.

Received: December 28, 2018
Revised: May 9, 2019
Accepted: November 14, 2019
Published: December 17, 2019

REFERENCES

Acar, M., Kocherlakota, K.S., Murphy, M.M., Peyer, J.G., Oguro, H., Inra, C.N., Jaiyeola, C., Zhao, Z., Luby-Phelps, K., and Morrison, S.J. (2015). Deep imaging of bone marrow shows non-dividing stem cells are mainly perisinusoidal. Nature *526*, 126–130.

Adolfsson, J., Borge, O.J., Bryder, D., Theilgaard-Mönch, K., Astrand-Grundström, I., Sitnicka, E., Sasaki, Y., and Jacobsen, S.E. (2001). Upregulation of Flt3 expression within the bone marrow Lin(-)Sca1(+)c-kit(+) stem cell compartment is accompanied by loss of self-renewal capacity. Immunity *15*, 659–669.

Aguilo, F., Avagyan, S., Labar, A., Sevilla, A., Lee, D.F., Kumar, P., Lemischka, I.R., Zhou, B.Y., and Snoeck, H.W. (2011). Prdm16 is a physiologic regulator of hematopoietic stem cells. Blood *117*, 5057–5066.

Anders, S., Pyl, P.T., and Huber, W. (2015). HTSeq—a Python framework to work with high-throughput sequencing data. Bioinformatics *31*, 166–169.

Arai, F., Hirao, A., Ohmura, M., Sato, H., Matsuoka, S., Takubo, K., Ito, K., Koh, G.Y., and Suda, T. (2004). Tie2/angiopoietin-1 signaling regulates hematopoietic stem cell quiescence in the bone marrow niche. Cell *118*, 149–161.

Ashburner, M., Ball, C.A., Blake, J.A., Botstein, D., Butler, H., Cherry, J.M., Davis, A.P., Dolinski, K., Dwight, S.S., Eppig, J.T., et al.; The Gene Ontology Consortium (2000). Gene Ontology: tool for the unification of biology. Nat. Genet. *25*, 25–29.

Balazs, A.B., Fabian, A.J., Esmon, C.T., and Mulligan, R.C. (2006). Endothelial protein C receptor (CD201) explicitly identifies hematopoietic stem cells in murine bone marrow. Blood *107*, 2317–2321.

Beerman, I., Bhattacharya, D., Zandi, S., Sigvardsson, M., Weissman, I.L., Bryder, D., and Rossi, D.J. (2010). Functionally distinct hematopoietic stem cells modulate hematopoietic lineage potential during aging by a mechanism of clonal expansion. Proc. Natl. Acad. Sci. U S A *107*, 5465–5470.

Benz, C., Copley, M.R., Kent, D.G., Wohrer, S., Cortes, A., Aghaeepour, N., Ma, E., Mader, H., Rowe, K., Day, C., et al. (2012). Hematopoietic stem cell subtypes expand differentially during development and display distinct lymphopoietic programs. Cell Stem Cell *10*, 273–283.

Bernitz, J.M., Kim, H.S., MacArthur, B., Sieburg, H., and Moore, K. (2016). Hematopoietic stem cells count and remember self-renewal divisions. Cell *167*, 1296–1309.e10.

Brennecke, P., Anders, S., Kim, J.K., Kołodziejczyk, A.A., Zhang, X., Proserpio, V., Baying, B., Benes, V., Teichmann, S.A., Marioni, J.C., and Heisler, M.G. (2013). Accounting for technical noise in single-cell RNA-seq experiments. Nat. Methods *10*, 1093–1095.

Buczacki, S.J., Zecchini, H.I., Nicholson, A.M., Russell, R., Vermeulen, L., Kemp, R., and Winton, D.J. (2013). Intestinal label-retaining cells are secretory precursors expressing Lgr5. Nature *495*, 65–69.

Cabezas-Wallscheid, N., Buettner, F., Sommerkamp, P., Klimmeck, D., Ladel, L., Thalheimer, F.B., Pastor-Flores, D., Roma, L.P., Renders, S., Zeisberger, P., et al. (2017). Vitamin A-retinoic acid signaling regulates hematopoietic stem cell dormancy. Cell *169*, 807–823.e19.

Cappell, S.D., Chung, M., Jaimovich, A., Spencer, S.L., and Meyer, T. (2016). Irreversible APC(Cdh1) inactivation underlies the point of no return for cell-cycle entry. Cell *166*, 167–180.

Carbon, S., Ireland, A., Mungall, C.J., Shu, S., Marshall, B., and Lewis, S.AmiGO Hub; Web Presence Working Group (2009). AmiGO: online access to ontology and annotation data. Bioinformatics *25*, 288–289.

Chen, J.Y., Miyanishi, M., Wang, S.K., Yamazaki, S., Sinha, R., Kao, K.S., Seita, J., Sahoo, D., Nakauchi, H., and Weissman, I.L. (2016). Hoxb5 marks long-term haematopoietic stem cells and reveals a homogenous perivascular niche. Nature *530*, 223–227.

Chu, I.M., Hengst, L., and Slingerland, J.M. (2008). The Cdk inhibitor p27 in human cancer: prognostic potential and relevance to anticancer therapy. Nat. Rev. Cancer *8*, 253–267.

Cotsarelis, G., Sun, T.T., and Lavker, R.M. (1990). Label-retaining cells reside in the bulge area of pilosebaceous unit: implications for follicular stem cells, hair cycle, and skin carcinogenesis. Cell *61*, 1329–1337.

de Boer, J., Williams, A., Skavdis, G., Harker, N., Coles, M., Tolaini, M., Norton, T., Williams, K., Roderick, K., Potocnik, A.J., and Kioussis, D. (2003). Transgenic mice with hematopoietic and lymphoid specific expression of Cre. Eur. J. Immunol. *33*, 314–325.

Dobin, A., Davis, C.A., Schlesinger, F., Drenkow, J., Zaleski, C., Jha, S., Batut, P., Chaisson, M., and Gingeras, T.R. (2013). STAR: ultrafast universal RNA-seq aligner. Bioinformatics *29*, 15–21.

Dykstra, B., Olthof, S., Schreuder, J., Ritsema, M., and de Haan, G. (2011). Clonal analysis reveals multiple functional defects of aged murine hematopoietic stem cells. J. Exp. Med. *208*, 2691–2703.

Egawa, T., Hanaoka, K., Koide, Y., Ujita, S., Takahashi, N., Ikegaya, Y., Matsuki, N., Terai, T., Ueno, T., Komatsu, T., and Nagano, T. (2011). Development of a far-red to near-infrared fluorescence probe for calcium ion and its application to multicolor neuronal imaging. J. Am. Chem. Soc. *133*, 14157–14159.

Ema, H., Takano, H., Sudo, K., and Nakauchi, H. (2000). In vitro self-renewal division of hematopoietic stem cells. J. Exp. Med. *192*, 1281–1288.

Foster, D.A., Yellen, P., Xu, L., and Saqcena, M. (2010). Regulation of G1 cell cycle progression: distinguishing the restriction point from a nutrient-sensing cell growth checkpoint(s). Genes Cancer *1*, 1124–1131.

Gazit, R., Mandal, P.K., Ebina, W., Ben-Zvi, A., Nombela-Arrieta, C., Silberstein, L.E., and Rossi, D.J. (2014). Fgd5 identifies hematopoietic stem cells in the murine bone marrow. J. Exp. Med. *211*, 1315–1331.

Giladi, A., Paul, F., Herzog, Y., Lubling, Y., Weiner, A., Yofe, I., Jaitin, D., Cabezas-Wallscheid, N., Dress, R., Ginhoux, F., et al. (2018). Single-cell characterization of haematopoietic progenitors and their trajectories in homeostasis and perturbed haematopoiesis. Nat. Cell Biol. *20*, 836–846.

Hayashi, T., Ozaki, H., Sasagawa, Y., Umeda, M., Danno, H., and Nikaido, I. (2018). Single-cell full-length total RNA sequencing uncovers dynamics of recursive splicing and enhancer RNAs. Nat. Commun. *9*, 619.

Howe, E.A., Sinha, R., Schlauch, D., and Quackenbush, J. (2011). RNA-seq analysis in MeV. Bioinformatics *27*, 3209–3210.

Hu, Y., and Smyth, G.K. (2009). ELDA: extreme limiting dilution analysis for comparing depleted and enriched populations in stem cell and other assays. J. Immunol. Methods *347*, 70–78.

Kiel, M.J., Yilmaz, O.H., Iwashita, T., Yilmaz, O.H., Terhorst, C., and Morrison, S.J. (2005). SLAM family receptors distinguish hematopoietic stem and progenitor cells and reveal endothelial niches for stem cells. Cell *121*, 1109–1121.

Kitamura, T., Koshino, Y., Shibata, F., Oki, T., Nakajima, H., Nosaka, T., and Kumagai, H. (2003). Retrovirus-mediated gene transfer and expression cloning: powerful tools in functional genomics. Exp. Hematol. *31*, 1007–1014.

Kozar, K., Ciemerych, M.A., Rebel, V.I., Shigematsu, H., Zagozdzon, A., Sicinska, E., Geng, Y., Yu, Q., Bhattacharya, S., Bronson, R.T., et al. (2004). Mouse development and cell proliferation in the absence of D-cyclins. Cell *118*, 477–491.

Laurenti, E., Frelin, C., Xie, S., Ferrari, R., Dunant, C.F., Zandi, S., Neumann, A., Plumb, I., Doulatov, S., Chen, J., et al. (2015). CDK6 levels regulate quiescence exit in human hematopoietic stem cells. Cell Stem Cell *16*, 302–313.

Li, L., and Clevers, H. (2010). Coexistence of quiescent and active adult stem cells in mammals. Science *327*, 542–545.

Loeffler, D., Wang, W., Hopf, A., Hilsenbeck, O., Bourgine, P.E., Rudolf, F., Martin, I., and Schroeder, T. (2018). Mouse and human HSPC immobilization in liquid culture by CD43- or CD44-antibody coating. Blood *131*, 1425–1429.

Luchsinger, L.L., de Almeida, M.J., Corrigan, D.J., Mumau, M., and Snoeck, H.W. (2016). Mitofusin 2 maintains haematopoietic stem cells with extensive lymphoid potential. Nature *529*, 528–531.

Luchsinger, L.L., Strikoudis, A., Danzl, N.M., Bush, E.C., Finlayson, M.O., Satwani, P., Sykes, M., Yazawa, M., and Snoeck, H.W. (2019). Harnessing hematopoietic stem cell low intracellular calcium improves their maintenance in vitro. Cell Stem Cell *25*, 225–240.e7.

Malumbres, M., Sotillo, R., Santamaría, D., Galán, J., Cerezo, A., Ortega, S., Dubus, P., and Barbacid, M. (2004). Mammalian cells cycle without the D-type cyclin-dependent kinases Cdk4 and Cdk6. Cell *118*, 493–504.

Martinsson, H.S., Starborg, M., Erlandsson, F., and Zetterberg, A. (2005). Single cell analysis of G1 check points-the relationship between the restriction point and phosphorylation of pRb. Exp. Cell Res. *305*, 383–391.

Mi, H., Muruganujan, A., Ebert, D., Huang, X., and Thomas, P.D. (2019). PANTHER version 14: more genomes, a new PANTHER GO-slim and improvements in enrichment analysis tools. Nucleic Acids Res. *47* (*D1*), D419–D426.

Montagnoli, A., Fiore, F., Eytan, E., Carrano, A.C., Draetta, G.F., Hershko, A., and Pagano, M. (1999). Ubiquitination of p27 is regulated by Cdk-dependent phosphorylation and trimeric complex formation. Genes Dev. *13*, 1181–1189.

Morita, S., Kojima, T., and Kitamura, T. (2000). Plat-E: an efficient and stable system for transient packaging of retroviruses. Gene Ther. *7*, 1063–1066.

Noda, S., Ichikawa, H., and Miyoshi, H. (2009). Hematopoietic stem cell aging is associated with functional decline and delayed cell cycle progression. Biochem. Biophys. Res. Commun. *383*, 210–215.

Oguro, H., Ding, L., and Morrison, S.J. (2013). SLAM family markers resolve functionally distinct subpopulations of hematopoietic stem cells and multipotent progenitors. Cell Stem Cell *13*, 102–116.

Oki, T., Nishimura, K., Kitaura, J., Togami, K., Maehara, A., Izawa, K., Sakaue-Sawano, A., Niida, A., Miyano, S., Aburatani, H., et al. (2014). A novel cell-cycle-indicator, mVenus-p27K-, identifies quiescent cells and visualizes G0-G1 transition. Sci. Rep. *4*, 4012.

Okuda, S., Watanabe, Y., Moriya, Y., Kawano, S., Yamamoto, T., Matsumoto, M., Takami, T., Kobayashi, D., Araki, N., Yoshizawa, A.C., et al. (2017). jPOSTrepo: an international standard data repository for proteomes. Nucleic Acids Res. *45* (*D1*), D1107–D1111.

Osawa, M., Hanada, K., Hamada, H., and Nakauchi, H. (1996). Long-term lymphohematopoietic reconstitution by a single CD34-low/negative hematopoietic stem cell. Science *273*, 242–245.

Potten, C.S., Hume, W.J., Reid, P., and Cairns, J. (1978). The segregation of DNA in epithelial stem cells. Cell *15*, 899–906.

Rappsilber, J., Mann, M., and Ishihama, Y. (2007). Protocol for micro-purification, enrichment, pre-fractionation and storage of peptides for proteomics using StageTips. Nat. Protoc. *2*, 1896–1906.

Rodriguez-Fraticelli, A.E., Wolock, S.L., Weinreb, C.S., Panero, R., Patel, S.H., Jankovic, M., Sun, J., Calogero, R.A., Klein, A.M., and Camargo, F.D. (2018). Clonal analysis of lineage fate in native haematopoiesis. Nature *553*, 212–216.

Rossi, D.J., Bryder, D., Zahn, J.M., Ahlenius, H., Sonu, R., Wagers, A.J., and Weissman, I.L. (2005). Cell intrinsic alterations underlie hematopoietic stem cell aging. Proc. Natl. Acad. Sci. U S A *102*, 9194–9199.

Sakamoto, H., Takeda, N., Arai, F., Hosokawa, K., Garcia, P., Suda, T., Frampton, J., and Ogawa, M. (2015). Determining c-Myb protein levels can isolate functional hematopoietic stem cell subtypes. Stem Cells *33*, 479–490.

Scheicher, R., Hoelbl-Kovacic, A., Bellutti, F., Tigan, A.S., Prchal-Murphy, M., Heller, G., Schneckenleithner, C., Salazar-Roa, M., Zöchbauer-Müller, S., Zuber, J., et al. (2015). CDK6 as a key regulator of hematopoietic and leukemic stem cell activation. Blood *125*, 90–101.

Seita, J., and Weissman, I.L. (2010). Hematopoietic stem cell: self-renewal versus differentiation. Wiley Interdiscip. Rev. Syst. Biol. Med. *2*, 640–653.

Shin, J.Y., Hu, W., Naramura, M., and Park, C.Y. (2014). High c-Kit expression identifies hematopoietic stem cells with impaired self-renewal and megakaryocytic bias. J. Exp. Med. *211*, 217–231.

Subramanian, A., Tamayo, P., Mootha, V.K., Mukherjee, S., Ebert, B.L., Gillette, M.A., Paulovich, A., Pomeroy, S.L., Golub, T.R., Lander, E.S., and Mesirov, J.P. (2005). Gene set enrichment analysis: a knowledge-based approach for interpreting genome-wide expression profiles. Proc. Natl. Acad. Sci. U S A *102*, 15545–15550.

Sugimura, R., He, X.C., Venkatraman, A., Arai, F., Box, A., Semerad, C., Haug, J.S., Peng, L., Zhong, X.B., Suda, T., and Li, L. (2012). Noncanonical Wnt signaling maintains hematopoietic stem cells in the niche. Cell *150*, 351–365.

Sun, J., Ramos, A., Chapman, B., Johnnidis, J.B., Le, L., Ho, Y.J., Klein, A., Hofmann, O., and Camargo, F.D. (2014). Clonal dynamics of native haematopoiesis. Nature *514*, 322–327.

Takizawa, H., Regoes, R.R., Boddupalli, C.S., Bonhoeffer, S., and Manz, M.G. (2011). Dynamic variation in cycling of hematopoietic stem cells in steady state and inflammation. J. Exp. Med. *208*, 273–284.

The Gene Ontology Consortium (2019). The Gene Ontology resource: 20 years and still GOing strong. Nucleic Acids Res. *47* (*D1*), D330–D338.

Ueda, T., Nakata, Y., Nagamachi, A., Yamasaki, N., Kanai, A., Sera, Y., Sasaki, M., Matsui, H., Honda, Z., Oda, H., et al. (2016). Propagation of trimethylated H3K27 regulated by polycomb protein EED is required for embryogenesis, hematopoietic maintenance, and tumor suppression. Proc. Natl. Acad. Sci. U S A *113*, 10370–10375.

Umemoto, T., Hashimoto, M., Matsumura, T., Nakamura-Ishizu, A., and Suda, T. (2018). Ca^{2+}-mitochondria axis drives cell division in hematopoietic stem cells. J. Exp. Med. *215*, 2097–2113.

van der Wath, R.C., Wilson, A., Laurenti, E., Trumpp, A., and Liò, P. (2009). Estimating dormant and active hematopoietic stem cell kinetics through extensive modeling of bromodeoxyuridine label-retaining cell dynamics. PLoS ONE *4*, e6972.

Weinreb, C., Wolock, S., and Klein, A.M. (2018). SPRING: a kinetic interface for visualizing high dimensional single-cell expression data. Bioinformatics *34*, 1246–1248.

Wilson, A., Laurenti, E., Oser, G., van der Wath, R.C., Blanco-Bose, W., Jaworski, M., Offner, S., Dunant, C.F., Eshkind, L., Bockamp, E., et al. (2008). Hematopoietic stem cells reversibly switch from dormancy to self-renewal during homeostasis and repair. Cell *135*, 1118–1129.

Wilson, N.K., Kent, D.G., Buettner, F., Shehata, M., Macaulay, I.C., Calero-Nieto, F.J., Sánchez Castillo, M., Oedekoven, C.A., Diamanti, E., Schulte, R., et al. (2015). Combined single-cell functional and gene expression analysis resolves heterogeneity within stem cell populations. Cell Stem Cell *16*, 712–724.

Wilson, A., Murphy, M.J., Oskarsson, T., Kaloulis, K., Bettess, M.D., Oser, G.M., Pasche, A.C., Knabenhans, C., Macdonald, H.R., and Trumpp, A. (2004). c-Myc controls the balance between hematopoietic stem cell self-renewal and differentiation. Genes Dev *18*, 2747–2763.

Yamamoto, R., Wilkinson, A.C., Ooehara, J., Lan, X., Lai, C.Y., Nakauchi, Y., Pritchard, J.K., and Nakauchi, H. (2018). Large-scale clonal analysis resolves aging of the mouse hematopoietic stem cell compartment. Cell Stem Cell *22*, 600–607.e4.

STAR★METHODS

KEY RESOURCES TABLE

REAGENT or RESOURCE	SOURCE	IDENTIFIER
Antibodies		
Anti-mouse CD150-PE (clone TC15-12F12.2)	BioLegend	Cat# 115904; RRID: AB_313683
Anti-mouse CD150-APC (clone TC15-12F12.2)	BioLegend	Cat# 115910; RRID: AB_493460
Anti-mouse CD150-BV605 (clone TC15-12F12.2)	BioLegend	Cat# 115927; RRID: AB_11204248
Anti-mouse CD48-APCcy7 (clone HM48-1)	BioLegend	Cat# 103431; RRID: AB_2561463
Anti-mouse CD48-BV421 (clone HM48-1)	BioLegend	Cat# 103427; RRID: AB_10895922
Anti-mouse CD34-Alexa700 (clone RAM34)	eBioscience	Cat# 56-0341-82; RRID: AB_493998
Anti-mouse CD34-eF450 (clone RAM34)	eBioscience	Cat# 48-0341-82; RRID: AB_2043837
Anti-mouse c-Kit-PEcy7 (clone 2B8)	BioLegend	Cat# 105814; RRID: AB_313223
Anti-mouse Sca-1-APC (clone D7)	BioLegend	Cat# 108112; RRID: AB_313349
Anti-mouse Sca-1-BV421 (clone D7)	BioLegend	Cat# 108127; RRID: AB_2563064
Anti-mouse Sca-1-BV785 (clone D7)	BioLegend	Cat# 108139; RRID: AB_2565957
Anti-mouse CD41-APC (clone MWReg30)	BioLegend	Cat# 133914; RRID: AB_11125581
Anti-mouse EPCR-APC (clone RCR-16)	BioLegend	Cat# 141506; RRID: AB_ 2561362
Anti-mouse ESAM-APC (clone 1G8/ESAM)	BioLegend	Cat# 136207; RRID: AB_ 2101658
Anti-mouse CD45.1-PE (clone A20)	BioLegend	Cat# 110708; RRID: AB_313497
Anti-mouse CD45.2-APCcy7 (clone 104)	BioLegend	Cat# 109824; RRID: AB_830789
Anti-mouse/human CD11b-biotine (clone M1/70)	BioLegend	Cat# 101204; RRID: AB_312787
Anti-mouse/human CD11b-PE (clone M1/70)	BioLegend	Cat# 101208; RRID: AB_312791
Anti-mouse/human CD11b-APC (clone M1/70)	BioLegend	Cat# 101212; RRID: AB_312795
Anti-mouse Gr-1-biotin (clone RB6-8C5)	BioLegend	Cat# 108404; RRID: AB_313369
Anti-mouse Gr-1-PE (clone RB6-8C5)	BioLegend	Cat# 108408; RRID: AB_313373
Anti-mouse Gr-1-APC(clone RB6-8C5)	Biolegend	Cat# 108412; RRID: AB_313377
Anti-mouse TER-119-biotin (clone TER-119)	BioLegend	Cat# 116204; RRID: AB_313705
Anti-mouse TER-119-PEcy7 (clone TER-119)	BioLegend	Cat# 116222; RRID: AB_2281408
Anti-mouse/human CD45R/B220-biotin (clone RA3-6B2)	BioLegend	Cat# 103204; RRID: AB_312989
Anti-mouse/human CD45R/B220-PEcy7 (clone RA3-6B2)	BioLegend	Cat# 103222; RRID: AB_313005
Anti-mouse CD5-biotin (clone 53-7.3)	BioLegend	Cat# 100604; RRID: AB_312733
Anti-mouse CD4-BV421 (clone GK1.5)	BioLegend	Cat# 100438; RRID: AB_11203718
Anti-mouse CD8a-BV421 (clone 53-6.7)	BioLegend	Cat# 100738; RRID: AB_11204079
Streptavidin MicroBeads	Miltenyi Biotec	Cat# 130-048-101
Streptavidin-PE	BioLegend	Cat# 405204
Streptavidin-PE/Dazzle 594	BioLegend	Cat# 405248
Streptavidin-BV421	BioLegend	Cat# 405225
Streptavidin-BV605	BioLegend	Cat# 405229
Rat anti-mouse Ki-67-APC (clone SolA15)	eBioscience	Cat# 17-5698-82 RRID: AB_2688057
Rat anti mouse Ki-67-eF450 (clone SolA15)	eBioscience	Cat# 48-5698-80 RRID: AB_11149124
Rabbit anti-mouse phospho-Rb (Ser807/811)-Alexa Fluor647 (clone D20B12)	Cell Signaling Technology	Cat# 8974S
Anti BrdU-PE (clone Bu20a)	BioLegend	Cat# 339812; RRID: AB_1626186

(*Continued on next page*)

Continued

REAGENT or RESOURCE	SOURCE	IDENTIFIER
Chemicals, Peptides, and Recombinant Proteins		
BrdU	Sigma-Aldrich	Cat# B5002
CaSiR-1 AM	GORYO Chemical	Cat# GC403
Fulo-8 AM	AAT Bioquest	Cat# 21081
Pluronic F-127	Biotium	Cat# 59005
Propidium Iodide	BioLegend	Cat# 421301
DAPI	BioLegend	Cat# 422801
Zombie NIR	BioLegend	Cat# 423105
StemSpan SFEM	STEMCELL Technologies	Cat# 9650
D-MEM (High-Glucose)	FUJIFILM Wako Chemical	Cat# 044-29765
D-MEM (High-Glucose)	GIBCO	Cat# 11995065
Fetal bovine serum	biowest	Cat# S1820-500
Fetal bovine serum	Sigma-Aldrich	Cat# 172012
Recombinant human TPO	R&D Systems	Cat# 288-TP
Recombinant human EPO	R&D Systems	Cat# 286-EP
Recombinant mouse SCF	R&D Systems	Cat# 455-MC
Recombinant mouse IL-3	R&D Systems	Cat# 403-ML
Recombinant mouse IL-6	R&D Systems	Cat# 406-ML
Recombinant mouse LIF	Merck	Cat# ESG1107
Geneticin Selective Antibiotic(G418 Sulfate)	GIBCO	Cat# 10131027
Penicillin-Streptomycin	Sigma-Aldrich	Cat# P4333
MEM Non-Essential Amino Acids Solution	GIBCO	Cat# 11140050
L-Glutamine	GIBCO	Cat# 25030081
2-Mercaptoethanol	Sigma-Aldrich	Cat# M7522
Lipopolysaccharide	Sigma-Aldrich	Cat# L4130
PD0332991 HCl	AdoQ BIOSCIENSE	Cat# A10701
Roscovitine	abcam	Cat# ab141847
PD98059	abcam	Cat# ab120234
SB203580	Cell signaling technology	Cat# #5633S
LY294002	abcam	Cat# ab120243
PP2	abcam	Cat# ab120308
Thapsigargin	abcam	Cat# ab120286
Calcimycin	abcam	Cat# ab120287
(±)-Verapamil Hydrochloride	Sigma-Aldrich	Cat# V-4629
RetroNectin	TaKaRa Bio	Cat# T100A
ACK Lysing Buffer	ThermoFisher Scientific	Cat# A1049201
Paraformaldehyde	FUJIFILM Wako Chemical	Cat# 162-16065
Triton X-100	FUJIFILM Wako Chemical	Cat# 162-24755
Goat Serum	Sigma-Aldrich	Cat# G9023
RNA lysis buffer	TaKaRa Bio	Cat# 635013
ERCC spike-ins	Life Technologies	Cat# 4456740
Klenow Fragment	New England Biolabs	Cat# M0212L
Protease inhibitor cocktail	Sigma-Aldrich	Cat# S8820
Tris (2-Carboxyethyl) phosphine Hydrochloride	Sigma-Aldrich	Cat# C4706
2-chloroacetamide	Sigma-Aldrich	Cat# C0267
ammonium bicarbonate	Sigma-Aldrich	Cat# 09830
Lysyl Endopeptidase	FUJIFILM Wako Chemical	Cat# 125-05061
Trypsin	Promega	Cat# V5280

(*Continued on next page*)

Continued

REAGENT or RESOURCE	SOURCE	IDENTIFIER
Critical Commercial Assays		
BrdU Staining Kit for Flow Cytometry APC	eBioscience	Cat# 8817-6600-42
Nextera XT DNA preparation kit	illumina	Cat# FC-131-1096
PrimeScript RT reagent kit	TaKaRa Bio	Cat# RR037A
LS Columns	Miltenyi Biotec	Cat# 130-042-401
Deposited Data		
Single cell RNA-seq data	Gene Expression Omnibus (https://www.ncbi.nlm.nih.gov/geo/)	GSE139013
Proteomics data	ProteomeXchange Consortium (http://proteomecentral.proteomexchange.org)	PXD012093
RNA-seq data	Gene Expression Omnibus (https://www.ncbi.nlm.nih.gov/geo/)	GSE138884
Experimental Models: Cell Lines		
PlatE	Morita et al., 2000	N/A
B6J/129 K1.1 ES cells	A gift from J. Takeda, Osaka University	N/A
Experimental Models: Organisms/Strains		
Mouse: *Rosa26*$^{mVenus\text{-}p27K\text{-}}$ mice	This study	https://ja.brc.riken.jp/BRC No. 109200
Mouse: Vav1-Cre transgenic mice	de Boer et al., 2003	N/A
Mouse: C57/B6J (Ly5.1) mice	Sankyo Labo Service Corporation, Tokyo, Japan	N/A
Mouse: C57/B6J (Ly5.2) mice	Japan SLC	http://www.jslc.co.jp/
Mouse: Kusabira-Orange transgenicmouse (KuO mouse)	Nakauchi Laboratory at University of Tokyo	https://linkinghub.elsevier.com/retrieve/pii/S0006291X13007870
Recombinant DNA		
pMYs-IRES-hNGFR mVenus-p27K$^-$ WT	This study	N/A
pMYs-IRES-hNGFR mVenus-p27K$^-$ T187A	This study	N/A
STOP-Rosa26TV targeting vector	a gift from Y. Sasaki, Kyoto University	N/A
Rosa26-STOP-mVenus-p27K$^-$	This study	N/A
Software and Algorithms		
Prism6	GraphPad Software	https://www.graphpad.com/scientific-software/prism/
Flowjo10	BD Biosciences	https://www.flowjo.com/solutions/flowjo
ELDA	Hu and Smyth, 2009	http://bioinf.wehi.edu.au/software/elda/
HTSeq	Anders et al., 2015	https://pypi.org/pypi/HTSeq/0.6.1
MeV	Howe et al., 2011	http://mev.tm4.org/#/welcome
Mascot v2.6.1	Matrix Science	http://www.matrixscience.com/
AmiGO2	Carbon et al., 2009	http://amigo.geneontology.org/amigo
CLC genomic workbench v11.0.0	QIAGEN	https://www.qiagenbioinformatics.com/products/clc-genomics-workbench/
GSEA	Subramanian et al., 2005	http://software.broadinstitute.org/gsea/index.jsp
Other		
BD FACSAria I Cell Sorter	BD Biosciences	N/A
BD FACSAria II Cell Sorter	BD Biosciences	N/A
BD FACSAria III Cell Sorter	BD Biosciences	N/A
BD FACSVerse Flow Cytometer	BD Biosciences	N/A
ECLIPSE Ti	Nikon	N/A

(*Continued on next page*)

Continued

REAGENT or RESOURCE	SOURCE	IDENTIFIER
EVOS FL Auto 2 Imaging System	Invitrogen	N/A
Hi-Seq 2500	illumina	N/A
Next-Seq system	illumina	N/A
Orbitrap Fusion LUMOS mass spectrometer	ThermoFisher Scientific	N/A

LEAD CONTACT AND MATERIALS AVAILABILITY

Information and requests for reagents may be directed to the lead contact Yosuke Tanaka (ytims@ims.u-tokyo.ac.jp). G_0 marker mouse line generated in this study have been deposited to Riken BioResource Research Center [B6.Cg-Gt(ROSA) 26Sor < tm1(mVenus/Cdkn1b < * >)Toki > , BRC No. 109200]. Plasmids generated in this study are available from the Lead Contact.

EXPERIMENTAL MODEL AND SUBJECT DETAILS

Mice

The *mVenus-p27K*$^-$ (G_0M; Oki et al., 2014) was subcloned into STOP-Rosa26TV targeting vector (a gift from Y. Sasaki (Kyoto University, Kyoto, Japan)) via H. Koseki (RIKEN, Yokohama, Kanagawa, Japan), resulting in the *Rosa26-STOP-mVenus-p27K*$^-$ allele (Figure S1A). Electroporation of the targeting vector to ESCs and screening of ESCs were performed as previously described (Ueda et al., 2016). Electroporation of ES cells were performed using 10^7 E14 KY1.1 ES cells and a 30 μg linearized vector. To verify homologous recombination in the mouse Rosa26 locus, individual clones were screened by 3′genomic PCR using P1 (5′-CTC TAT GGC TTC TGA GGC GGA AAG AAC CAG-3′) and P2 (5′-CTT TAA GAG CCA TGG CAA TGT TCA AGC AGG-3′) primers, followed by a 5′ Southern blot using EcoRI-digested DNA and a 5′external probe (Figure S1A). Correctly targeted ESCs were microinjected into blastocysts derived from C57BL/6 × BDF1 mice, and chimeric male mice were crossed with C57BL/6 female mice to transmit the mutant allele to progeny. After ten generations of backcross with C57BL/6, mice harboring the *mVenus-p27K*$^-$ knock-in allele were crossed with Vav1-Cre transgenic mice (de Boer et al., 2003). Female C57BL/6-Ly5.2 (Ly5.2) and male C57BL/6-Ly5.1 (Ly5.1) mice were purchased from Japan SLC (Shizuoka, Japan) and Sankyo-Lab Service (Tsukuba, Japan), respectively. Kusabira-Orange mice (KuO mice; a gift from Nakauchi lab.) served as donors. Eight- to twelve-week-old male and female mice served for experiments unless otherwise noted. All mice were housed at 22 ± 2°C and 12:12 hr light: dark cycle. The experiments were approved by the Committee on the Ethics of Animal Experiments, University of Tokyo.

Cell lines

PlatE (Morita et al., 2000) was cultured in D-MEM (Wako) containing 10% fetal bovine serum (FBS) (biowest). PlatE was authenticated by short-tandem repeat analyses and tested for mycoplasma contamination in our laboratory. E14 KY1.1 ES cells () was cultured in () containing (). All cell lines were cultured at 37°C and 5% CO_2.

METHOD DETAILS

Antibodies, Flow Cytometry and Cell Purification

BM hematopoietic cells were isolated from femurs and tibias by flushing and depleted of red blood cells by ACK Lysing Buffer (Thermo Fisher Scientific). Cells were stained with the appropriate dilution of fluorochrome- and/or biotin-conjugated antibodies and 4',6-diamidino-2-phenylindole (DAPI) or Propidium iodide (PI) for dead cell exclusion and analyzed on FACSVerse flow cytometer and FASCAria (BD Biosciences). The following antibodies were used: fluorescent CD150 (clone TC15-12F12.2), CD48 (clone HAM48-1), CD34 (clone RAM34), c-Kit (clone 2B8), Sca-1 (clone D7), CD45.1 (clone A20), CD45.2 (clone 104), CD11b (clone M1/70), Gr-1 (clone RB6-8C5), TER119 (clone TER-119), CD45R/B220 (clone RA3-6B2), CD5 (clone 53-7.3), CD4 (clone GK1.5), CD8a (clone 53-6.7), biotinylated lineage antibodies (CD11b, Gr-1, TER119, CD45R/B220, CD5) (BioLegend), and Ki-67 (clone SolA15) (eBiosciences). Biotinylated antibodies were detected with fluorochrome conjugated streptavidin (BioLegend).

LT-HSCs, ST-HSCs, MPP2s, MPP3/4 s, CMPs, GMPs and MEPs were defined by immune-phenotype as follows; LT-HSCs; Lineage marker-negative Sca-1$^+$ c-Kit$^+$ CD150$^+$ CD48$^-$, ST-HSCs; Lineage marker-negative Sca-1$^+$ c-Kit$^+$ CD150$^-$ CD48$^-$, MPP2s; Lineage marker-negative Sca-1$^+$ c-Kit$^+$ CD150$^+$ CD48$^+$, MPP3/4 s; Lineage marker-negative Sca-1$^+$ c-Kit$^+$ CD150$^-$ CD48$^+$, CMPs; Lineage marker-negative Sca-1$^-$ c-Kit$^+$ FcγR$^-$ CD34$^+$, GMPs; Lineage marker-negative Sca-1$^-$ c-Kit$^+$ FcγR$^+$ CD34$^+$, MEPs; Lineage marker-negative Sca-1$^-$ c-Kit$^+$ FcγR$^-$ CD34$^-$.

To isolate $G_0M^{high/low/neg}$ LT-HSCs, LT-HSCs were separated by the intensity of mVenus signal and sorted by FACSAria cell sorter. The sorted cells were collected into ice-cold PBS for reconstitution assays, into StemSpan SFEM (STEMCELL Technologies Inc.) for repopulation assay, time-lapse live-cell imaging and mass analysis, and into RNA lysis buffer (TaKaRa Bio Inc.) for RNA-Seq. To

isolate $[Ca^{2+}]_c^{high}/[Ca^{2+}]_c^{low}$ G_0M^{high} LT-HSCs, G_0M^{high} LT-HSCs were further-separated by CaSiR-1 (GORYO Chemical) and sorted in the same way.

For intracellular flow cytometric analysis, lineage marker-negative fraction was fixed with 4% PFA (Wako) after surface marker staining. After fixation, cells were permeabilized and blocked with 0.2% Triton X-100 (Wako) and 10% Goat Serum (Sigma) in PBS for 60 min. Then, cells were stained on ice for 30 min with the following primary and secondary antibodies; APC-conjugated anti-Ki-67 antibody (Clone: 16A8, BioLegend), and Alexa Fluor 647-conjugated anti-pRb (Ser807/811) antibody (Clone: D20B12, Cell Signaling Technology).

BrdU Treatment and Label-Retaining Assays

In vivo 5-bromodeoxy-uridine (BrdU, Sigma) labeling was performed as previously described (Wilson et al., 2004). BrdU was administered through the drinking water at 800 μg/ml to mice for 14 days. After 14 days BrdU administration, mice were maintained without BrdU for 60 days or 90 days. After 60 days or 90 days, mice were sacrificed and analyzed. BrdU staining was quantitated by flow cytometry (Wilson et al., 2004) by combining surface staining to define each BM subset with intracellular staining using the BrdU-APC staining kit following the manufacturer's instructions (BD Biosciences) or PE-conjugated anti-BrdU antibody (Clone: Bu20, BioLegend).

Calcium Measurement

The CaSiR-1 AM (GORYO Chemical) (Egawa et al., 2011) and Fulo8-AM (AAT Bioquest) allows the qualitative measurement of calcium levels in cytoplasm of intact living cells . Lineage marker-negative fraction were stained for 1hr under 5% CO_2/ 37°C using 0.3μM CaSiR-1 AM or 0.3μM Fulo8-AM in HBSS buffer with 0.02% pluronic F127 (Biotium) after surface marker staining. The intensities of CaSiR-1 AM or Fulo8-AM were analyzed by flow cytometry.

In vivo Treatment

The hG_0 mice were intraperitoneally injected with 100 mg/kg PD0332991 (AdoQ BIOSCIENCE), 5mg/kg Lipopolysaccharide (LPS) (Sigma), 30 mg/kg Verapamil (Sigma) or PBS. Injection volume was 200 μl per mouse. Twenty-four hr after intraperitoneally injection, mice were sacrificed and analyzed the intensities of G_0M and CaSiR1-AM by flow cytometry with surface staining to define each BM subset.

Bone Marrow Transplantation

The following hematopoietic cells (CD45.1) were transplanted to lethally irradiated mice (9.5 Gy, CD45.2) by tail vein injection; 2×10^5 whole BM cells from Vav1-Cre^-;Rosa-STOP-mVenus-$p27K^-$ mice or Vav1-Cre^+;Rosa-STOP-mVenus-$p27K^-$ mice (hG0 mice) (to examine normal hematopoiesis in hG_0 mice), 100 LT-HSCs (defined as LSK $CD150^+CD48^-$ G_0M^{high}/ G_0M^{low}/ G_0^{neg}, Sca-1^{high}/ Sca-1^{low} or $[Ca^{2+}]_c^{high}/[Ca^{2+}]_c^{low}$) from hG_0 mice (to compare their HSC potential), 100 LT-HSCs cultured with DMSO, 0.1 μM Thapsigargin or 1 μM Calcimycin for 24 hr from KuO mouse (to examine effects of upregulation of $[Ca^{2+}]_c$ for HSC potential). For the secondary transplantation assay, 5×10^6 whole BM cells from primary recipient mice 16 weeks after transplantation were transplanted into lethally irradiated (9.5 Gy) CD45.2 mice. In all transplantation experiments, contribution of $CD45.1^+$ or KuO^+-donor cells were monitored in peripheral blood at 4, 8, 12 and 16 weeks post-transplantation using the following antibodies; PE-conjugated anti-CD45.1 antibody (Clone: A20, BioLegend), APC-Cy7-conjugated anti-CD45.2 antibody (Clone: 104, BioLegend), APC-conjugated anti-Gr-1 antibody (Clone: RB6-8C5, BioLegend), APC-conjugated anti-CD11b antibody (Clone:M1/70, BioLegend), PE-Cy7-conjugated anti-CD45R/B220 antibody (Clone:RA3-6B2, BioLegend), BV421-conjugated anti-CD4 antibody (Clone:GK1.5, BioLegend) and BV421-conjugated anti-CD8a antibody (Clone:53-6.7, BioLegend). Verapamil was administered through the drinking water at 1 mg/ml to recipient mice after transplantation. Frequencies of HSCs which contribute to LT-HSCs fraction in primary recipient mice were analyzed by Extreme Limiting Dilution Analysis (ELDA) (Hu and Smyth, 2009).

HSC Culture

HSC culture media consists of StemSpan SFEM (STEMCELL Technologies Inc.) supplemented with 50 ng/ml recombinant mouse SCF (R&D systems), 50 ng/ml recombinant human TPO (R&D systems). 20 μM PD98059 (Abcam), 10 μM Ly294002 (Abcam), 5 μM PP2 (Abcam), 20 μM SB203580 (Cell Signaling Technology), 1 μM PD0332991 (AdoQ BIOSCIENCE) and 20 μM roscovitine (Abcam) were added in culture. After 24 hr culture, the intensity of G_0M was analyzed by flow cytometry.

Viral Transduction

Retroviruses were produced by transient transfection into Plat-E packaging cells with retroviral constructs using the calcium-phosphate method (Kitamura et al., 2003). Mixture of 20 ng plasmid (20 μl), 2.5 M $CaCl_2$ (50 μl) and filtered water (430 μl) to 2 × HeBS (500 μl) dropwise while vortexing. Mixture of these solutions was added to Plat-E which were seeded in a 10 cm dish (2.0×10^6 cells/dish) 18 hr before transfection. After 24 hours, remove medium by aspiration and add fresh 5 mL of DMEM (Wako)/10% FBS (biowest). After 24 hours, supernatant was retrieved and centrifuged for 4 hr at 15,000 g. After centrifuge, remove medium by aspiration and add fresh 50 μl of StemSpan SFEM (STEMCELL Technologies Inc.). Retrovirus transduction to the cells was performed using RetroNectin (TaKaRa Bio Inc). LT-HSCs were sorted from C57BL/6-Ly5.2 (Ly5.2) mouse and then cultured for

12hrs before infection. One-hundred μl of 25μg/ml RetroNectin in PBS was courted to 96 well flat bottom plate for overnight at 4°C. RetroNectin was removed and then blocking was performed with an 2% bovine serum albumin (BSA, Fraction V) in PBS for 30 minutes at room temperature. BSA solution was removed and the plate was washed once with PBS. After removing the wash solution, LT-HSCs and retrovirus were put onto plate. After 24 hr viral transduction, the intensity of G_0M was analyzed by flow cytometry.

Time-lapse Live-cell Imaging of LT-HSC

LT-HSCs (defined as LSK $CD150^+CD48^-G_0M^{high/low/neg}$ $[Ca^{2+}]_c^{high/low}$) from 8-12 weeks old hG_0 mice were sorted into 96-well U bottom plates by single cell/well or 96-well flat bottom plates courting with 0.5 μg/ml of purified anti-CD43 antibody (clone S11, BioLegend) as previously described (Loeffler et al., 2018), in StemSpan SFEM (STEMCELL Technologies Inc.) with 50 ng/ml SCF (R&D systems) and TPO (R&D systems). Plates were gas-tight sealed with adhesive tape after preincubation at 5% CO_2 / 37°C for at least 0-12 hr. Time-lapse live-cell imaging was performed using a ECLIPSE Ti (Nickon) or Invitrogen EVOS FL Auto 2 Imaging System (Thermo Fisher Scientific) at 37°C. Phase contrast images were acquired every 30 min using a 10x phase contrast objective, and an camera (at 1388x1040 pixel resolution). The first mitosis of the purified LT-HSCs was defined as time of first division. The time between first mitosis and second mitosis was defined as time of second division. Dead cells were easily depicted by their shrunk, non-refracting appearance with immobility. All cell tracking was done by scientists; the current analysis does not rely on data generated by an unsupervised computer algorithm for automated tracking.

Single-cell RNA-Seq

We performed scRNA-Seq as described previously (Wilson et al., 2015). Single-cells were sorted by FACS directly into individual wells of a 96-well plate containing lysis buffer, and libraries were prepared using the Illumina Nextera XT DNA preparation kit. Pooled libraries were run on the Illumina Hi-Seq 2500 and reads aligned using STAR (Dobin et al., 2013). HTSeq (Anders et al., 2015) was run to assign mapped reads to Ensembl genes. Mapped reads were normalized using size factors as described (Brennecke et al., 2013). We estimated technical noise (Brennecke et al., 2013) and fitted the relation between mean read counts and squared coefficient of variation using ERCC spike-ins (Life Technologies). Genes for which the squared coefficient

RNA-Seq

We performed RNA-Seq as described previously (Hayashi et al., 2018) with minor modification. In brief, using 100 sorted cells, the first strand of cDNA was synthesized by using PrimeScript RT reagent kit (TaKaRa Bio Inc.) and not-so random primers. Following the synthesis of the first strand, the second strand was synthesized by using Klenow Fragment (3′, −5′, exo-; New England Biolabs Inc.) and complement chains of not-so random primers. Using purified double-strand cDNA, the library for RNA-Seq was prepared and amplified using Nextera XT DNA sample Prep kit (Illumina Inc.). These prepared libraries were sequenced on Next-Seq system (Illumina Inc.), according to the manufacturer's instruction. In addition, each obtained read was mapped to the reference sequence "GRCm38/mm10" using CLC genomic workbench v11.0.0 (QIAGEN), and expression levels were normalized and subjected to the statistical analyses based on EdgeR. Transcriptome data were subjected to GSEA using GSEA v3.0.0 software, available from the Broad Institute (Subramanian et al., 2005). All Gene sets were obtained from the database of Broad Institute unless otherwise stated. Principle component analysis, hierarchal clustering analysis and visualization of gene expression or protein level were performed by Multi expression Viewer (MeV) (Howe et al., 2011).

Proteomic Analysis

Seventeen thousand and five hundred cells of G_0M^{high}, G_0M^{low} and G_0M^{neg} LT-HSCs were sorted to 10 μL of lysis buffer (8 M Urea, 100 mM Tris-HCl at pH 8.5, protease inhibitor cocktail (Sigma), 10 mM Tris (2-Carboxyethyl) phosphine Hydrochloride (Sigma) and 40 mM 2-chloroacetamide (Sigma)) and sonicate for 20 min on ice. Proteins solubilized were 2-fold diluted by 50 mM ammonium bicarbonate (Sigma) and digested with Lys-C (Wako) for 3 hr at 37°C, and the digest were 2-fold diluted again and further digested with trypsin (Promega) for overnight at 37°C. The digested solution was acidified with 0.5% Trifluoroacetic acid (final concentration) and desalted using SDB-XC StageTips (Rappsilber et al., 2007). The digested peptides were analyzed by nanoLC/MS/MS using an Orbitrap Fusion LUMOS mass spectrometer (Thermo Fisher Scientific, Bremen, Germany) which were connected to a Thermo Ultimate 3000 pump and a HTC-PAL autosampler (CTC Analytics, Zwingen, Switzerland). Peptides were separated by self-pulled needle columns (150 mm length × 100 μm ID, 6 μm opening) packed with ReproSil-Pur C18-AQ 3 μm (Dr. Maisch, Ammerbuch, Germany). The injection volume was 5 μL and the flow rate was 500 nL/min. The mobile phases consisted of (A) 0.5% acetic acid and (B) 0.5% acetic acid and 80% ACN. Two-step linear gradient of 10−4 0% B in 60 min, 40%–99% B in 5 min, 99% B for 10 min was employed for fractionated samples. Spray voltages of 2400 V was applied. The mass scan ranges for Orbitrap system was *m/z* 300−1500, with an automatic gain control value of 4.00e + 05, a max injection time of 50 ms and detected at a mass resolution of 60,000 at *m/z* 200 in Orbitrap analyzer. The precursor ions were selected in a top speed mode within 3 s cycle time for each MS scan and subsequent MS/MS scans with an automatic gain control value of 5.00e + 04 and a max injection time of 100 ms. Dynamic exclusion was set for 20 s with a 10 ppm. The normalized HCD was set to be 30 and detected at a mass resolution of 15,000 at *m/z* 200 in Orbitrap analyzer. Proteins were identified by Mascot v2.6.1 (Matrix Science, London, UK) against mouse Swiss-Prot database (version 2017_4, 16,916 sequences) with a precursor mass tolerance of 10 ppm, a fragment ion mass tolerance of 20 ppm, and strict trypsin specificity allowing for up to 2 missed cleavage. Carbamidomethylation of cysteine was set as a fixed modification, methionine oxidation

and protein N-terminal acetylation were allowed as variable modifications. Proteomics data were subjected to Gene Ontology term analysis using AmiGO2 (The Gene Ontology Consortium, 2019; Ashburner et al., 2000; Carbon et al., 2009; Mi et al., 2019).

QUANTIFICATION AND STATISTICAL ANALYSIS

Statistical analyses were performed by the unpaired and two-tailed Student's t test or by analysis of variance (ANOVA) with Dunnett's or Turkey's post hoc test after testing for normal distribution and equal variance. GraphPad Prism 6 was used for these statistical analyses. The numbers of samples were presented as n in the figure legends. All data are presented as mean ± SEM in the figures. Significance levels were set at $p^* < 0.05$, and $p^{**} < 0.01$.

DATA AND CODE AVAILABILITY

The single cell RNA-seq and RNA-seq data have been deposited to Gene Expression Omnibus (GEO) (https://www.ncbi.nlm.nih.gov/geo/) with the dataset identifier GEO: GSE139013 and GEO: GSE138884 respectively. The MS raw data and analysis files have been deposited to the ProteomeXchange Consortium (http://proteomecentral.proteomexchange.org) via the jPOST partner repository (https://jpostdb.org) (Okuda et al., 2017) with the dataset identifier ProteomeXchange Consortium: PXD012093.